THE RELATIONSHIP OF INTERFACIAL ENERGY TO GRAPHITE SHAPE IN THE Fe-C SYSTEM

BY

EDWARD BRUCE HAWBOLT
B.A.Sc., The University of British Columbia, 1960

A THESIS SUBMITTED IN PARTIAL FULFILMENT OF
THE REQUIREMENTS FOR THE DEGREE OF
MASTER OF APPLIED SCIENCE

in the Department
of
METALLURGY

We accept this thesis as conforming to the standard required from candidates for the degree of MASTER OF APPLIED SCIENCE.

Members of the Department of Metallurgy

THE UNIVERSITY OF BRITISH COLUMBIA

August 1964

In presenting this thesis in partial fulfilment of the requirements for an advanced degree at the University of British Columbia, I agree that the Library shall make it freely available for reference and study. I further agree that permission for extensive copying of this thesis for scholarly purposes may be granted by the Head of my Department or by his representatives. It is understood that copying or publication of this thesis for financial gain shall not be allowed without my written permission.

Department of Metallurgy

The University of British Columbia,
Vancouver 8, Canada

Date September 4, 1964

ABSTRACT

The relationship between surface energy and precipitated graphite form in Fe-C alloys was examined in this thesis. Surface tension and contact angle data were obtained using the sessile drop technique. Carbon saturated, puron iron crucibles were melted on pyrolytic graphite, the effect of time, temperature (1300-1600°C) and additions of Ni, Mn, S or Ce being examined. The graphite form was established by metallographic examination.

An average γ_{LV} of 1152 dynes/cm was determined for the Fe-C alloys (4.6% C) at approximately 1300°C, the average contact angle being 128°.

No significant change occurred with additions of Ni (0.85%) and Mn (1.65%). Additions of S lowered the surface energy and increased the equilibrium contact angle. Ce additions had a similar effect although a direct comparison with the Fe-C alloys could not be made as different temperatures were used. However, the interfacial energy difference apparently increased with increasing Ce content, implying an adsorption of Ce to the graphite-melt interface.

The change from the flake to the nodular form was accomplished in several transition stages, the interfacial energy differences being small, indicating a marked dependence on the solidification and growth conditions.

ACKNOWLEDGEMENT

The author gratefully acknowledges the advice and guidance given by Professor W. M. Armstrong throughout the investigation. The author is especially indebted to Mrs. A. M. Armstrong for assistance in interpreting and preparing the final manuscript. Thanks are also extended to R. G. Butters, R. J. Richter and P. R. Musil for their technical assistance and to fellow graduate students and other faculty members for their helpful discussions.

Financial support was received from the Defence Research Board of Canada under Grant No. 7501-02 and from the Aluminium Laboratories in the form of a graduate research fellowship. This support is gratefully acknowledged.

TABLE OF CONTENTS

continued...

Table of Contents Continued...

LIST OF FIGURES

List of Figures Continued...

LIST OF TABLES

LIST OF APPENDICES

I. INTRODUCTION

A. General Discussion of Cast Irons

Cast irons comprise a large group of Fe-C alloys with carbon in the range 1.7 to 6.7 wt.%. In the solidified alloy the carbon may occur as a carbide or as free graphite. Moreover, the graphite may assume a variety of forms. Since the physical properties of a composite material are strongly dependent on its microstructure both the shape and distribution of the relatively weak, dispersed graphite phase are of major significance in determining the final strength characteristics of a cast iron.

The microstructure is dependent on the carbon content, the alloy and impurity content, the cooling rate during and after freezing and the conditions of heat treatment. While the general effects of these variables on the resulting microstructure are well known, the details of the formation and growth mechanisms operating are still not completely understood.

The most pronounced change in the shape of the graphite phase is from the flake form of grey iron to the spheroidal form of nodular iron. In the production of nodular or ductile iron a spheroidizing agent, either Mg as a NiMg or FeSiMg alloy, or Ce as mischmetal (an alloy of rare earths containing 50% Ce) is added to a grey iron composition following tapping of the melt from the furnace. The graphite in the solidified alloy is thereby changed from a flake to a spheroid with an accompanying increase in strength and ductility. This change in graphite shape has been related to an increase in the graphite-melt interfacial energy[1,2,3].

It is the relationship between the surface energy and the resulting graphite form which will be examined in this thesis.

B. Background Theory

1. The Surface Tension Parameter[4]

The most general approach to variations of the free energy of a homogeneous bulk phase can be considered in terms of the following basic thermodynamic relationship:

$$dF = -SdT + VdP + \sum \mu_i \, dn_i$$

where dF is the change in the Gibbs free energy
S is the entropy
T is the absolute temperature
V is the volume
P is the pressure
μ_i is the chemical potential of component i
n_i is the number of moles of component i

In a two phase system a surface of separation will be present and thus an additional energy term will be required. This additional energy is associated with the change in the surroundings of the surface atoms. A simple but descriptive picture of a metal surface has been proposed by Uhlig[5]. It is considered to be a portion of the lattice where atoms have fewer than the usual number of nearest neighbours. The strength of each interatomic bond must therefore be greater. Since the strength per bond is directly associated with the degree of attraction of the atoms, the characteristic atomic radius or the distance of closest approach must be less. It is the restraint of the parent lattice to this tendency for closer approach that gives rise to what is called surface tension (γ).

To increase the area of a surface by an infinitesimal amount, dA, at constant T, P and composition, these bonds must be stretched and the work required is γdA. Thus the surface free energy change can be written:

$$dF^s = -S^s dT + V^s dP + \gamma\, dA + \Sigma \mu_i\, dn_i^s \text{ ✱}$$

and at constant T, P and n_i

$$\frac{\partial F^s}{\partial A} = \gamma$$

or the surface free energy/unit area and the surface tension are identical in the liquid, leading to the dimensions of γ being dynes/cm, i.e., force/unit length or ergs/cm^2, i.e., energy/unit area.

2. The Relationship of Surface Energy to Precipitating Form

It is known that nucleating shapes can be controlled or at least modified by variations in the interfacial energy[6,7].

Turnbull[8] and Turnbull and Fisher[9] have derived the following theoretical expressions for the rate of homogeneous and heterogeneous nucleation in the solidification of a one component system:

$$I_v = K_v \exp\left[\frac{-a\gamma^3}{(\Delta F_v)^2 kT}\right]$$

and

$$I_s = K_s \exp\left[\frac{-a\gamma^3 f(\theta)}{(\Delta F_v)^2 kT}\right]$$

where I_v and I_s are the rates of homogeneous and heterogeneous nucleation respectively, γ is the interfacial energy between the solidifying crystal and the parent liquid, ΔF_v is the free energy change per unit volume for the transition of the liquid to the solid, a is the constant dependent on the nucleus shape, $f(\theta)$ is a function of the equilibrium contact angle between the nucleus and the nucleating phase (for heterogeneous nucleation),

---

✱ In most developments $V^s \longrightarrow 0$ since the interface is assumed planar.

K_V and K_S are constants dependent on the nucleus shape, surface area of the critical nucleus, free energy of activation for transport of an atom from the liquid to the crystal, temperature of the system, etc.

These relationships illustrate the significance of the interfacial energy with respect to the rate of nucleation. The number of growing nuclei is dependent on the rate of nucleation which in turn is associated with the degree of undercooling[6]. It is specifically these two properties, the number of growing nuclei and the degree of undercooling, which may affect the rate of growth and hence the shape of the solidifying form. The interfacial energy is thus an important parameter when considering changes in the shape of a precipitating material.

Although the nucleating form is controlled by such thermodynamic parameters as the interfacial energy, the final shape observed is also dependent on the growth conditions following nucleation.

Although the solid-liquid interfacial energy is the parameter of interest, its direct experimental determination is not possible at this time. The best approach to the problem can only indicate the direction and magnitude of changes in the interfacial energy due to additions of various elements.

3. The Effect of Solute Additions on Interfacial Energy

Solute atoms can change interfacial energies by preferentially adsorbing on the interface in question. If the interatomic forces are such that the solute element is rejected by the matrix atoms, the solute may become preferentially concentrated at the surface of the material - hence the term, surface active element. The resulting excess surface concentration

would change the surface tension of the alloy. Thus those elements that exhibit a positive deviation from Raoult's law should be surface active to varying degrees.

The theoretical approach to excess surface concentrations and the resulting effect on the interfacial energy makes use of Gibbs Adsorption Theory[10]. For a binary alloy this has the general form

$$-d\gamma = \Gamma_1 \, d\mu_1 + \Gamma_2 d\mu_2$$

where $d\gamma$ is the change in the interfacial energy
Γ_i is the excess interfacial concentration of component i
$d\mu_i$ is the change in the chemical potential of component i

This reduces to

$$\Gamma_2 = -\frac{\partial \gamma}{\partial \mu_2}$$

at a chosen interface position where the excess concentration of the solvent atom is zero. By replacing the chemical potential μ_1 by RT ln a_1, the simplified form of the adsorption equation is obtained

$$\Gamma_2 = -\frac{1}{RT}\frac{\partial \gamma}{\partial \ln a_2}$$

where a_2 is the activity of component 2
R is the gas constant
T is the absolute temperature

Where the solute obeys Henry's law the mole fraction may be used in place of the activity,

$$\text{i.e.} \quad \Gamma_2 = -\frac{C_2 \partial \gamma}{RT \, \partial C_2}$$

where C_2 is the mole fraction of component 2.

Since it is possible to determine experimentally the direction and magnitude of change of the interfacial energy, i.e., $d\gamma$, it is also possible to determine whether surface adsorption is occurring. Thus the conditions present at the interface can be examined and related to other properties, in this thesis, the precipitating form.

C. Review of Previous Work

Since little work has been done in which surface energies are related to the graphite form, it is necessary to consider the two initially as separate parameters. This section will deal first with the surface tension data reported for Fe-C alloys, including the effect of various alloying elements, and secondly with the graphite form and its relationship to composition and solidification conditions. The third and final section will review the data reported in which graphite form and surface energy have been related.

1. Surface Tension Measurements

Considerable interest has recently been directed to obtaining surface tension values for materials of either high purity or precisely known composition. This has been necessitated by the poor reproducibility of the early work. Quantitatively comparable data is now obtainable due to the appreciation of the marked effect of minor concentrations of surface active materials. The effect of minor elements is especially important in iron and its alloys since two of the major contaminants are S and O, both of which are very surface active. Only that data recently reported will be considered, as good reproducibility is attained.

It has been shown that the surface tension of Fe-C alloys is independent of the carbon concentration over the range 0 to 4.5 wt.%[2,11-14].

Dyson[13] has established that sulphur additions lower the γ_{LV} of liquid iron and predicts 1920 dynes/cm for the γ_{LV} of sulphur-free, pure iron in agreement with published values for pure iron and iron-carbon alloys[2,11,12,14].

Although carbon is not surface active in pure Fe-C alloys, its presence does influence the γ_{LV} of Fe-C-S alloys. To compare the results of several investigations Keverian[2] plotted the γ_{LV} versus activity of sulphur as shown in Figure 1a. Although the effect of carbon on the S activity is not evident in this plot, Figure 1b. shows the data of Kozakevitch[15] plotted in a slightly different manner clearly illustrating the effect of the carbon.

Additions to iron of elements which are not surface active, such as Ni, produce a change in the surface tension of the alloy as a linear function of the atomic per cent of the alloying addition[16].

Kaufman and Whalen[17] have reported γ_{LV} values for ternary Fe-1.5%C-Ni alloys having a wide range of Ni additions. The carbon had little effect on the change of γ_{LV} with Ni additions. A similar effect is expected for Fe-C alloys containing small additions of Mn.

No quantitative results have been published concerning the effect of Ce additions on the surface tension of pure iron . However, Minkoff[18] has predicted a decrease in γ_{LV} with additions of Ce. It is a well established fact that Ce is a strong sulphide former and with additions of Ce to iron containing S, the primary action of the Ce is to remove the sulphur[2,19].

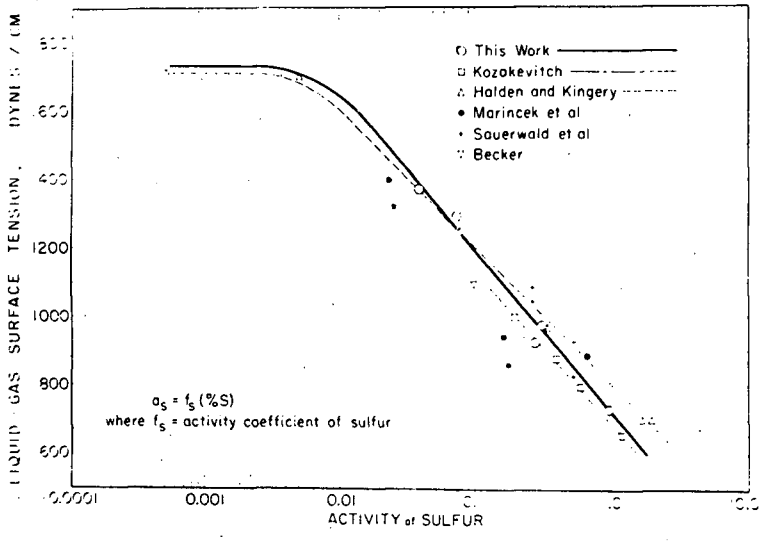

Figure 1a. Comparison of Surface Tension Data With Respect to S Activity (Keverian[2])

Effect of Sulfur on the Surface Tension of Liquid Iron-Carbon Alloys at 1450°C (2642°F).

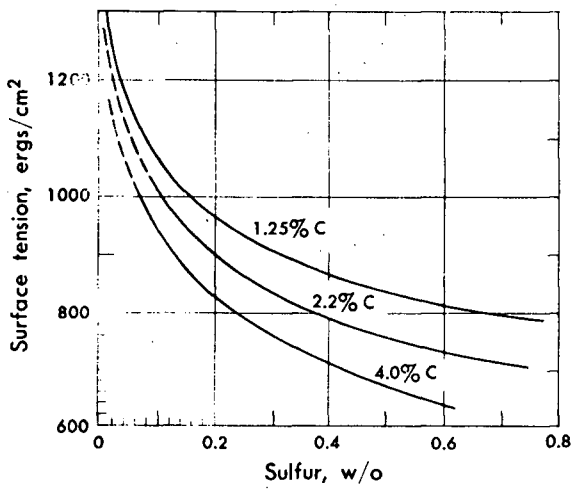

Figure 1b. Kozakevitch's Data Showing the Effect of C and S, (Kozakevitch[15])

Keverian[2] has shown that additions of Ce to an iron containing sulphur cause an increase in γ_{LV}.

2. Solidification of a Hypereutectic Iron

An extensive review of the solidification and graphitization of cast irons has been compiled by Boyles[20], Morrogh and Williams[21] and Loper and Heine[22,23]. Although this thesis deals with the simple Fe-C system in the hypereutectic C range containing only minor additions of S, Ni, Mn and Ce and not a cast iron, the solidification characteristics are very similar[20].

The main addition to the Fe-C system to produce a cast iron is Si, the major effect of which is to create a range over which the eutectic solidifies and to stabilize the graphitic form of carbon.

Figure 2. illustrates the Fe-C phase diagram and contains the equilibrium solidification conditions for both the graphite and the Fe_3C system.

In cooling a hypereutectic liquid below the liquidus temperature proeutectic graphite (kish graphite) forms in the melt. With decreasing temperature this form will develop and may float to the surface due to its lower specific gravity[24]. At the eutectic arrest temperature a eutectic of austenite and graphite solidifies on a spheroidal crystallization front called a eutectic cell. These cells are generally nucleated by the kish graphite already present. The ends of the growing flake graphite remain in contact with the surrounding liquid. The sequence of development is shown in the sketches of Figure 3.

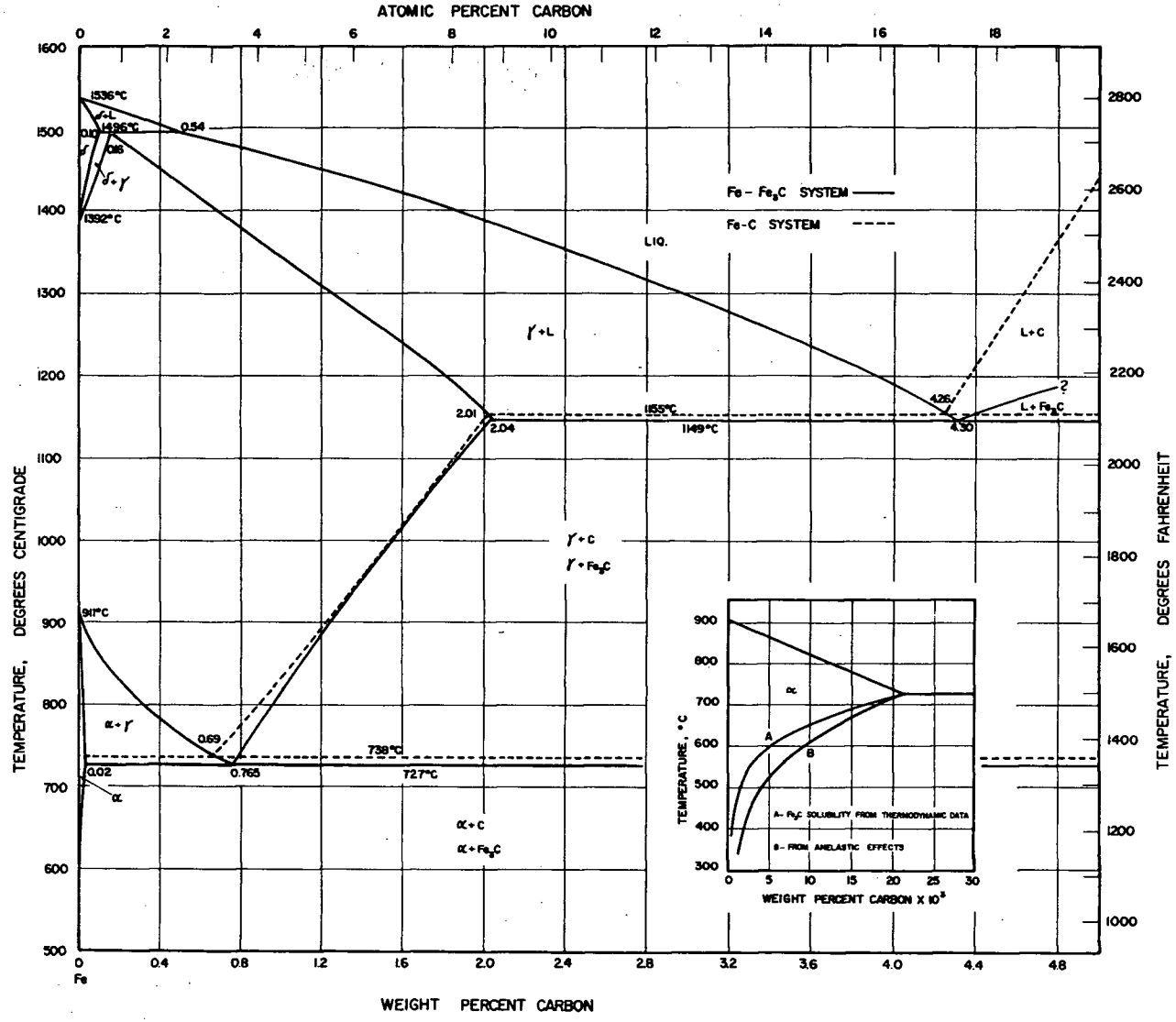

Figure 2. Fe-C Phase Diagram (Kirkaldy and Purdy[47])

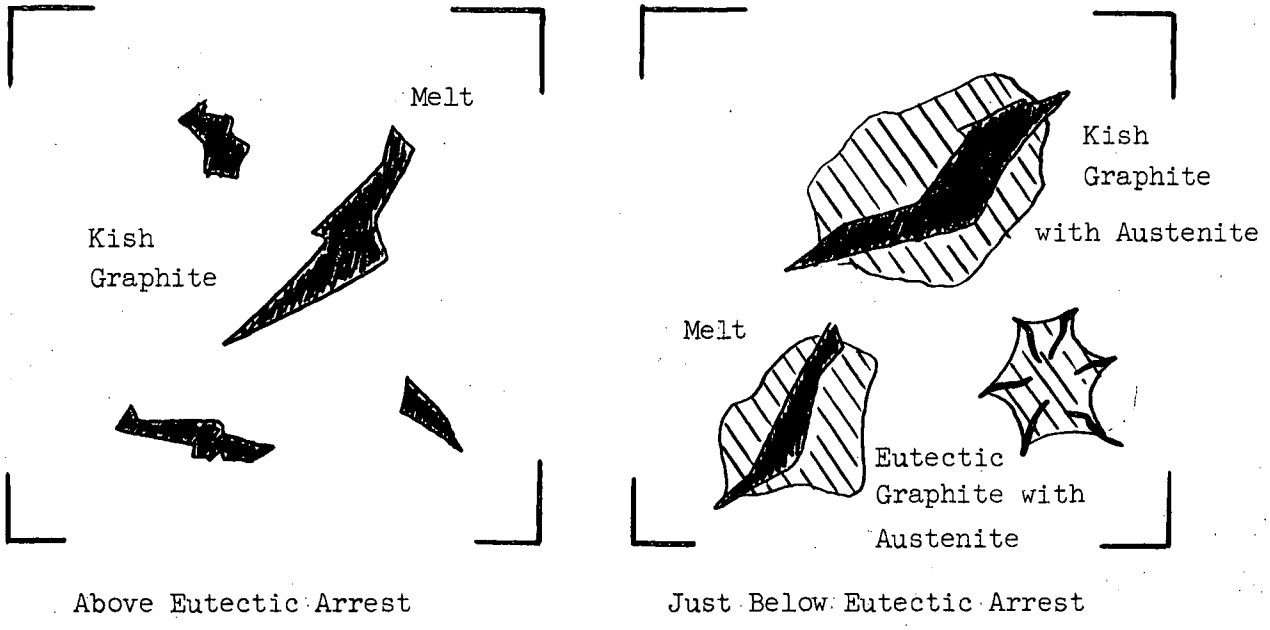

Figure 3. Graphite Development Above and Below the Eutectic Arrest

On completion of the eutectic solidification the structure consists of irregular kish graphite flakes and smaller eutectic flake graphite, the matrix being austenite.

With decreasing temperature to the eutectoid, the solubility of carbon in austenite decreases producing some proeutectoid graphite which is usually deposited on the flakes already present. Below the eutectoid temperature the austenite decomposes to either α plus graphite or α plus Fe_3C, depending on the relative stabilities of the two systems. Generally the Fe_3C transformation is predominant as the diffusion rate of carbon is relatively low at these temperatures. No observable changes occur as the structure is cooled to room temperature.

Increasing the cooling rate produces a finer, randomly oriented eutectic graphite, type D in the A.S.T.M. Graphite Form Designation[25].

a. Effects of Alloy Additions on the Graphite Form

i. Sulphur

Garber[26] and Williams[27] have reported that increasing the sulphur content to 0.028 wt.% increases the size and amount of the primary flake graphite and decreases the amount of undercooled D-type eutectic graphite. A coarse flake existed at 0.028 % and persisted as the predominant form up to 0.1 wt.%. A transition from flake to mesh to compact aggregate to free carbide occurred with increase in the sulphur content up to 0.6 wt.%.

While observing the effect of S additions, Garber also noted a carbon deposit on the surface of the ingots, increasing in amount with increasing S. He interpreted this ejection of carbon from the melt as being a surface phenomenon in which graphite was not wetted by the melt.

Boyles[20] has shown that sulphur is concentrated in the eutectic liquid during the formation of the primary dendrites (hypoeutectic iron) and during freezing of the eutectic is further concentrated in the eutectic cell boundaries. This sulphur is finally precipitated as FeS inclusions.

ii. Manganese

Williams[27] has shown that increasing the manganese content of Fe-C alloys increases the tendency for the structure to solidify white.

iii. Nickel[28]

Solubility of carbon in molten iron is lowered as the nickel content is increased, 0.2% for a 4% Ni addition. An increase occurs in the eutectic temperature, 25°F for a 4% Ni addition, reducing the tendency for the eutectic to solidify with Fe_3C as the stable phase.

Nickel is readily soluble in solid iron, enlarging the temperature-composition range in which austenite is stable. This results in a lowering of the critical transformation temperature of austenite, about 40°F for each % Ni added.

It is difficult to discuss the effects of specific additions when explaining the cast iron structure. It suffices to say that the observed microstructure is a result of the specific composition and cooling rate of the alloy.

b. Effect of Cooling Rate on Structure

Morrogh[29] has graphically illustrated the effect of cooling rate on the relative stability of the austenite-graphite, austenite-Fe_3C transformation (Figure 4).

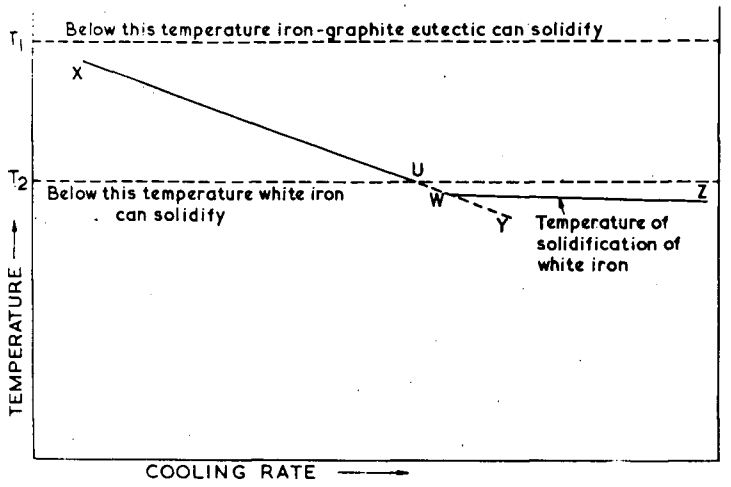

Figure 4. Relative Stabilities of the Graphite and Carbide as Affected By the Cooling Rate (Morrogh[29])

With increasing cooling rates the temperature at which the graphite eutectic forms becomes progressively lower. In Figure 4, T_1 corresponds to the equilibrium cooling conditions below which the γ -graphite transition occurs, whereas below T_2, this being the melting point of the white iron

eutectic, the γ-Fe_3C will predominate. Increasing the cooling rate causes the eutectic transition temperature to follow a curve of form XU. At a cooling rate and transformation temperature equal to W, white iron will be the eutectic second component. With a further increase in the cooling rate the eutectic solidification temperature decreases slightly according to WZ.

The tendency for an iron to solidify white is also affected by the composition - Si and Mn increase this tendency while Ni decreases it. In addition, superheating will cause a melt to undercool thereby increasing the Fe_3C stability.

3. Solidification of a Hypereutectic Nodular Iron

Since no information is available on the effect of adding Ce to a pure Fe-C alloy, it is necessary to restrict our discussion to an Fe-C-Si alloy. When Ce is added to such a melt, small graphite nuclei appear above the liquidus temperature, their presence having been established by rapid quenching tests[22,23,30,31]. These nuclei have only been observed in irons in which the graphite precipitates in the spheroidal form. Loper and Heine[22] have developed a schematic representation of the temperature range of nucleation and growth for the various graphite forms (Figure 5).

With decreasing temperature the nuclei develop into larger spheroids. These are separated from the liquid by a thin shell of austenite. The thickness of this shell remains constant up to the eutectic start temperature[30], although the nodules grow in size. Over the eutectic solidification range the nodule size continues to increase as does the surrounding austenitic shell.

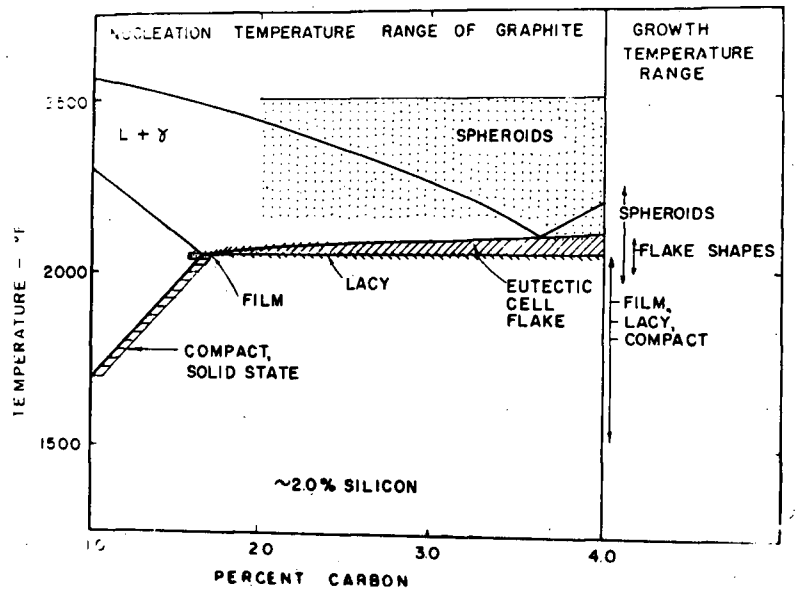

Figure 5. Nucleation Range of the Various Graphite Forms (Loper and Heine[22])

For growth of the nodule to continue, carbon must diffuse through the austenite shell and iron must diffuse in the opposite direction. With increasing shell thickness the diffusion time increases, impeding growth. The driving force necessary for the reaction to proceed is supplied by a decrease in the temperature. Such a solidification process requires a greater eutectic solidification range, being approximately twice that for a comparable grey iron[22].

Although some nodules remain dormant during the eutectic solidification no satisfactory explanation has been developed to explain this effect. Subsequent cooling below the eutectic to the eutectoid generally results in precipitation of the excess carbon on the graphite present.

It has often been reported that supercooling is a requirement for the formation of spheroidal graphite[1,3]. However, in the experiments previously discussed, the graphite nodules were present above the eutectic solidification temperature and thus were not associated with supercooling. The widening of the eutectic solidification range is a result of and not the cause of solidification in the spheroidal form.

Morrogh[32] has illustrated the development characteristics of a nodule, as shown in Figure 6.

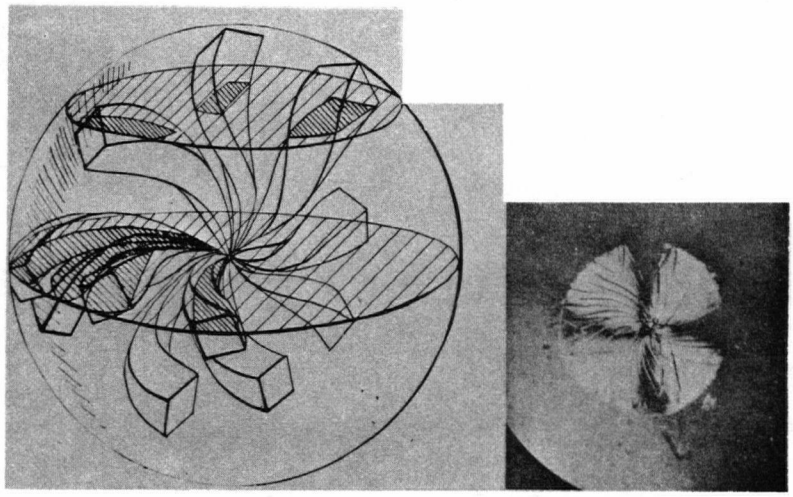

Figure 6. Growth Characteristics of a Graphite Nodule (Morrogh[32])

The nodule is essentially a radial development of the basal plane of the hexagonal graphite[33].

4. Relationship Between Interfacial Energy and Graphite Form

The change from the flake to the spheroidal form has been related to an increase in the graphite-melt interfacial energy[2,3,18]. It is thought that such an increase would necessitate a higher driving force for solidification to occur, acting as a barrier to nucleation. Keverian[2] showed that Ce additions to an Fe-C-S alloy increased the surface tension, reflecting the desulphurizing power of Ce. However no associated increase in the graphite-melt interfacial energy could be determined.

Such an approach implies that nodular graphite is related to supercooling. This could not account for the presence of nuclei above the eutectic temperature.

D. Sessile Drop Technique[4]

It is obvious that if one wishes to establish the interface conditions present during graphitization, one must examine the graphite-melt interface. However, it is not possible to measure directly the surface energy of such an interface. Using the techniques available one is able, at best, to determine the direction and magnitude of change of this parameter.

The approach used in this work is related to the shape of a liquid drop resting on an inert base plate. This is known as the sessile drop technique and permits evaluation of the surface tension of the liquid, γ_{LV}, and the contact angle through the drop, ϕ. The experimental difficulties and errors inherent in this approach are outlined in Appendix I.

The shape of a liquid drop on a horizontal, inert surface is determined by the balance between the surface tension which attempts to create a spherical drop, i.e., the lowest surface area/unit volume, and the gravitational force which tries to lower the potential energy of the mass by flattening the liquid.

The equation of the sectional outline of such a drop is a second order differential which has been numerically solved to four places of decimal by Bashforth and Adams[34]. By use of their tabulated solutions it is possible to determine γ_{LV} and the contact angle ϕ.

It is necessary to measure the parameters x, x^1, z , z^1 shown in Figure 7. From these parameters and Bashforth and Adams' tables, two further parameters, β and b can be obtained (as shown in the thesis of D. J. Rose[35]), from which

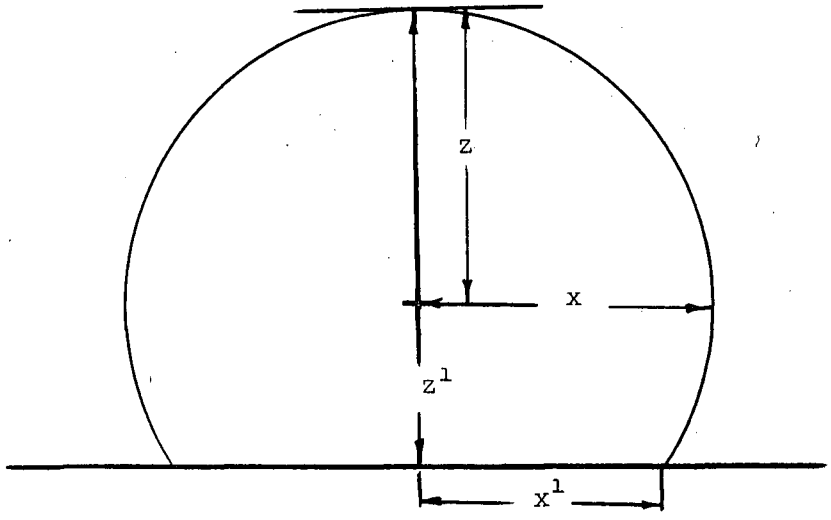

Figure 7. The Sessile Drop Parameters of Interest For γ_{LV} and ϕ Determination

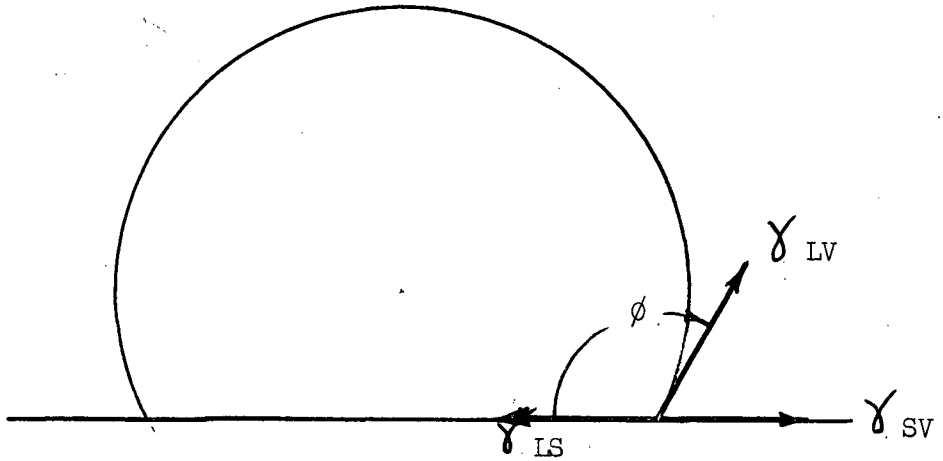

Figure 8. Silhouette of a Liquid Drop on an Inert Base Showing Those Forces Present at the Interface Which Have Horizontal Components

$$\gamma_{LV} = \frac{g\ d\ b^2}{\beta\ m^2}$$

where g is the gravity constant
d is the density
m is the magnification of the drop from which the parameters were taken

and ϕ, the interior contact angle, can be determined. The fact that both γ_{LV} and ϕ can be measured as independent parameters is a distinct advantage in this experimental procedure. By applying the values obtained for γ_{LV} and ϕ, and changes in these values, to Young's Equation,

$$\gamma_{LS} = \gamma_{SV} - \gamma_{LV} \cos \phi$$

this being a balance of the horizontal components of the surface forces shown in Figure 8, and by having a knowledge of, or by making certain assumptions for γ_{SV}, the direction and magnitude of change of γ_{SL} can be determined.

E. Choice of System and Aim of Investigation

The complexity of commercial cast irons restricts their use in any fundamental investigation. To reduce the many composition variables it is necessary to examine simple binary, or at most, ternary alloys. To study graphitization therefore, the pure Fe-C binary is the obvious choice. However, as this system may contain the metastable carbide it is also necessary to employ conditions which ensure the stability of the free graphite form. This was accomplished by air cooling the carbon saturated puron iron in a reduced pressure of 10^{-5} mm Hg.

Since changes in the primary graphite shape were to be related to the graphite-melt interfacial energy present during graphitization, it was necessary to maximize these changes to ensure their detection. The transition from the flake to the nodular form was thus examined.

It has been reported that a nodule occurs at an early stage in its growth in contact with the melt, and is a radial development of the basal plane of the hexagonal graphite system. Thus, to determine the interfacial conditions present during the formation of a nodule, the graphite basal plane-melt interface had to be included in the system under investigation.

Pyrolytic graphite is composed of parallel, misoriented layers of the graphite basal plane[36]. Thus by melting Fe-C binary alloys on a pyrolytic graphite plate the melt-graphite basal plane interface could be studied. To ensure that no reaction occurred at this interface, complying with those conditions necessary for the sessile drop application, the Fe-C alloys were carbon saturated. In addition, since it was necessary that the energy parameters be obtained during graphitization, the alloy had to contain a greater amount of carbon than that required for saturation at the melting temperature. Thus, the binary Fe-C alloy was saturated with C at 1500°C and quenched from this temperature to retain the carbon content.

Since it is only possible to determine the direction and magnitude of change of the solid-liquid interfacial energy it was necessary to make solute additions to the basic alloy. The elements Ce, S, Ni and Mn were chosen for the following reasons:

- Ce was employed as the spheroidizing agent to effect the change from the flake to the nodular form.

- Sulphur additions were made since the presence of, or rather the removal of sulphur has been associated with nodule formation.

- Nickel and manganese were used because both are sulphide formers, although much weaker than Ce, and both are generally present in commercial cast irons.

The original plan was to study the effect of sulphur additions and additions of sulphur plus Ce, Ni or Mn on the surface energy and graphite form. However, preliminary experiments indicated that the examination of additions of the single elements to the Fe-C system would be more profitable.

II. EXPERIMENTAL

A. Materials Used

Sessile drop experiment were conducted using carbon-saturated puron iron as the basic alloy, Ce, S, Ni and Mn as addition agents, and pyrolytic graphite as the base plate.

The Fe-C alloy was prepared by induction heating puron iron in a spectrographic grade graphite crucible to 1500°C in a vacuum of 10^{-5} mm Hg. This temperature was held for 10 minutes to ensure completion of the reaction, the power was shut off and the sample was allowed to cool.

Crucibles 0.25" X 0.20" were machined from this alloy, the bottom surface being bevelled to ensure an advancing interface upon melting, and the center being drilled to hold alloy additions. Drops of approximately 0.5 gms were obtained by this procedure.

Master alloys were prepared to ensure better control of the additives. Ni and Mn master alloys were prepared from 99.9% metals, these being added to puron iron and melted under 10^{-5} mm pressure in spectrographic grade graphite crucibles.

The Ce master alloy was prepared using 99.9% Ce and puron iron, the melting being carried out in a sealed spectrographic grade crucible, held under similar vacuum conditions. The S master alloy was prepared by heating puron iron in a spectrographic grade graphite crucible to 1050°C under a flow of H_2S.

The analyses of the materials used and the master alloys prepared are reported in Table I.

Pyrolytic graphite base plates 5/8" X 5/8" were cut from 3/16 X 4 X 5" sheets supplied by the General Electric Laboratories. Details concerning the production and properties of pyrolytic graphite are recorded in Appendix II.

TABLE I.

Analyses of Materials Used and Alloys Prepared

Material or Alloy	Al	Cr	Cu	Ce	Fe	Mg	Mn	Mo	Ni	Si	Ti	V	C	S
Puron Iron ✱	0.005	0.0008	<0.002	N.D.	Matrix	<0.0008	<0.002	<0.002	<0.004	<0.001	0.0005	0.002	0.068	<0.01
	0.0003	<0.0001	0.0004	<0.02	Matrix	0.0001	<0.0005	0.001	0.0008	0.0003	0.002	0.001	0.082	<0.01
Spectrographic Grade Graphite used for molds for preparing alloys:														
	0.0003	<0.0001	0.0004	<0.02	0.1	0.00005	<0.0005	0.0008	0.0002	0.0009	0.005	0.002	Matrix	<0.01
Fe-C Alloy 1	0.0002	<0.0001	0.0008	<0.02	Matrix	0.0002	<0.0005	0.001	0.0008	0.0003	0.003	0.001	5.4	<0.01
Fe-C Alloy 4	0.0002	<0.0001	0.0006	<0.02	Matrix	0.0001	<0.0005	0.002	0.03	0.02	0.002	0.002	5.49	<0.01
Fe-C Alloy 5	0.0001	<0.0001	0.001	<0.02	Matrix	0.0003	<0.0005	0.002	0.01	0.01	0.003	0.001	5.57	<0.01
Master Alloys -														
Fe-S							-		-					42.3
Fe-C-Ce							-		-				5.7	0.53
Fe-C-Mn							18.0		-				5.25	
Fe-C-Ni							-		10.87				5.20	0.034
Pyrolytic Graphite	0.0008	<0.0001	0.0008	-	0.00005	0.0001	<0.0005	<0.002	0.0002	0.0005	0.00005	<0.0005	Matrix	0.01

✱ Analysis supplied with material, others being obtained from Coast Eldridge Engineers. All metallics not listed were undetected.

B. Apparatus

The sessile drop experiments were conducted in the induction apparatus described in detail in a thesis by D. J. Rose[35]. A molybdenum susceptor 5/8" X 0.005" X 3" was suspended in the center of a 65 mm O.D. vycor tube. The samples were placed in the center of the susceptor, no radiation shields being required. A Lepel (Model T-10-3) high-frequency induction generator supplied the power to the furnace and temperatures were measured at 45° to the furnace axis. A Hartmann and Braun disappearing filament optical pyrometer was employed, the readings being taken through a mirror which could be rotated into position between the end of the furnace and the photographing lens. By comparing these temperatures with values simultaneously obtained using a W-WRe thermocouple fitted into the pyrolytic graphite sample a temperature correction of + 55° was observed over the temperature range of interest.

A vacuum of 10^{-5} mm Hg was maintained for all of the tests.

The drop shape was recorded using a Bell and Howell 8 mm movie camera combined with a lens assembly which permitted photographing the complete image at the film size and at a distance of about 2 1/2 feet. The apparatus including the vertical coil employed to prepare the master alloys is shown in Figure 9.

C. Experimental Procedure

Experiments of 20 minutes duration were conducted, the effect of time after melting, temperature and alloy addition being recorded.

γ_{LV} and contact angle data were obtained from prints of the projected images magnified approximately 10 times.

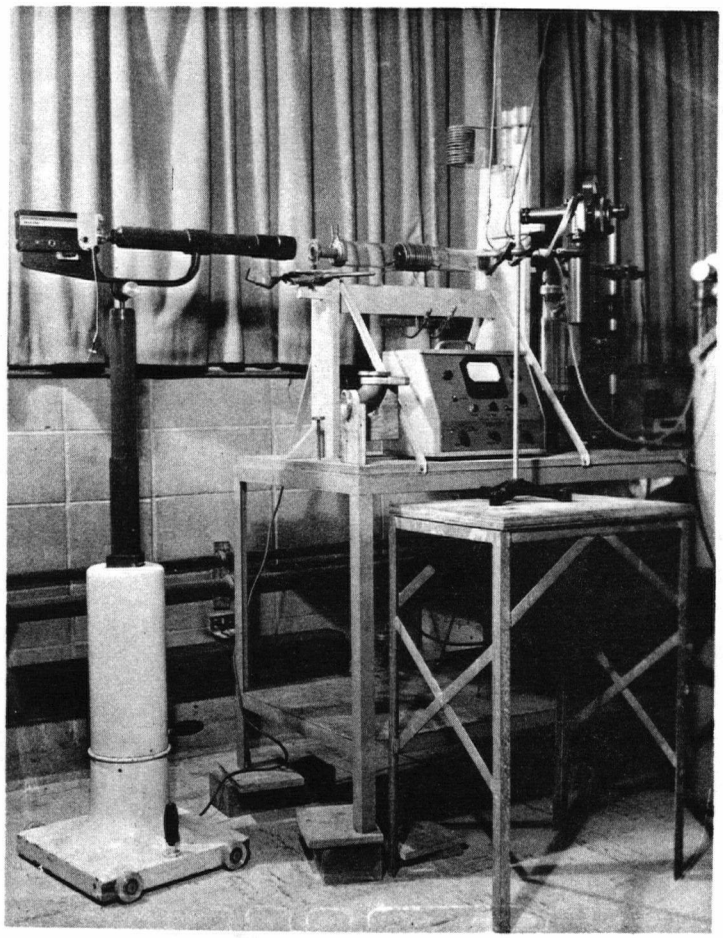

Figure 9. Equipment Used for Alloy Preparation and Sessile Drop Experiments

The graphite form was obtained from polished sections of the solidified drops - the samples were mounted in 828 epon and polished with 6 μ and 1 μ diamond paste.

Much care was exercized in handling the materialsto avoid contamination. The base plates were rinsed in acetone, dipped into concentrated HCl, washed in alcohol and dried just prior to their use. During and after washing, all materials were handled by metal tweezers. A similar cleaning cycle was followed for the iron crucibles.

When additions were made, the material was placed in the crucible following the cleaning schedule, the crucible diameter and weight was recorded, the materials then being placed in the experimental apparatus. When a vacuum of 1 μ was obtained, a picture was taken for magnification determination and hydrogen gas was introduced to the system. This flushing was repeated several times to ensure the removal of any gaseous contaminants. A pressure of 500 mm of Hg was finally held and the materials were heated to red heat, the ensuing hydrogen flashing removing the surface oxides. The system was then pumped down to 10^{-5} mm Hg and the temperature was slowly increased to the melting point of the alloy ($\approx$ 1280°C). Photographs were taken at the start of melting and periodically through the heating cycle, the time being recorded. All samples were quenched from 1600°to ensure similar cooling conditions and hence comparable microstructures.

Analyses of the solidified drops were obtained to guard against any serious contaminations occurring during the experiment.

III. RESULTS

A. Sessile Drop Results

1. Basic Iron-Carbon Alloy

The parameters x, z, x^1 and z^1 were obtained from the enlarged negatives and the surface tensions and contact angles were determined, the results being listed in Appendix III. Density values were obtained by considering the drop to be C saturated at each temperature[38] and using the reported relationship between temperature, density and carbon concentration[39]. The average γ_{LV} and contact angle for the Fe-C alloy is shown in Table II. An estimation of the standard deviation for three tests is also included to illustrate the range of results in any one test, the calculations being included in Appendix IV.

The effect of time and temperature on the contact angle is illustrated in Figure 10. Only those ϕ values for temperatures less than 1345°C are plotted since above this temperature significant wetting of the base occurred, as shown in the photographs included in Figure 10. As the contact angle approaches 90° it becomes virtually impossible to obtain the desired z parameter. Surface tensions were only determined from high angle drops for this reason, the equilibrium angle for temperatures up to 1345°C being sufficient to permit the parameter measurement.

No consistent variation of γ_{LV} with time or contact angle change was observed, the data being available in Appendix III.

Table III illustrates the pronounced effect of ± 0.01" variation in the z parameter on the resulting γ_{LV}.

Figure 11. shows the wetting characteristics of puron iron at 1415°C as compared to carbon saturated puron iron at 1400° and 1600°C.

TABLE II.

Average Surface Tension and Contact Angle of the Fe-C, Fe-C-Ni and Fe-C-Mn Alloys

Exp. No.	Average γ_{LV} (dynes/cm)	± 1 σ	No. of Calculations Averaged	Temp. °C	Approx. Equilibrium Angle
Fe-C Alloys					
14	1163	150	29	1325	126
19	1074	116	26	1325	128
20 a) Statistical	1079	120	20	1280	-
b) Effect of Time	1064	-	10	1280	-
27	1206	-	5	1290	132
28	1197	-	4	1335	122
29	1234	-	4	1345	129
35	1116	-	7	1335	129
Average	1152	Max. Spread 957 to 1307	105	1290 to 1345	128
Fe-C-Ni Alloy (0.85 wt.% Ni)					
45	1135	-	8	1285	118
Fe-C-Mn Alloy (1.65 wt.% Mn)					
43	1261	-	8	1330	127

TABLE III.

Effect of ± 0.01" Variation in the x and z Parameters on γ_{LV} e.g. Seq 1-380 of Experiment 20

	x	z	x/z	γ_{LV} (dynes/cm)	Variation
	1.065	0.977	1.090	1021	-
z + 0.01"	1.065	0.987	1.079	1153	+ 132
z - 0.01"	1.065	0.967	1.101	900	- 121

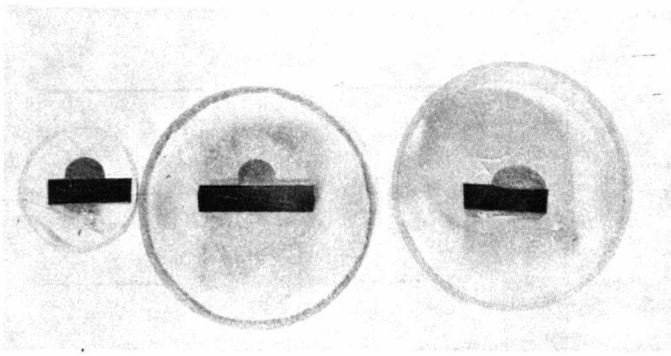

Figure 11. Wetting Characteristics of a) Fe-C at 1600°C $\theta \simeq 90°$ (left)
b) Fe-C at 1400°C $\theta \simeq 115°$
c) Puron iron at 1415°C
$\theta \simeq 75°$ (right)

2. Effect of Ni and Mn Additions

Although separate Ni and Mn additions were made, 0 to 0.85% Ni and 0 to 1.65 wt.% Mn, no significant changes in γ_{LV} or ϕ were noted, the data pertaining to the maximum additions being reported in Figure 10 and Table II.

3. Effect of Sulphur Additions

The surface tension and contact angle were difficult to obtain for these alloys. With the addition of sulphur, the solubility of graphite in iron is decreased. The excess graphite was precipitated out on the surface of the drop thereby distorting the true drop parameters. Although it was known that sulphur had this effect on carbon it was thought that the excess graphite would precipitate onto the primary graphite present within the structure. Figure 12 illustrates the effect of sulphur on the drop silhouette, plate c) showing the sectioned drop and the actual drop parameters as compared to the graphite outline noted in plate b). In this case parameter measurements were taken from the solidified drop and an approximate surface tension was calculated. This surface graphite precipitation is no doubt the same carbon deposition noted by Garber[26] in his sulphur experiments.

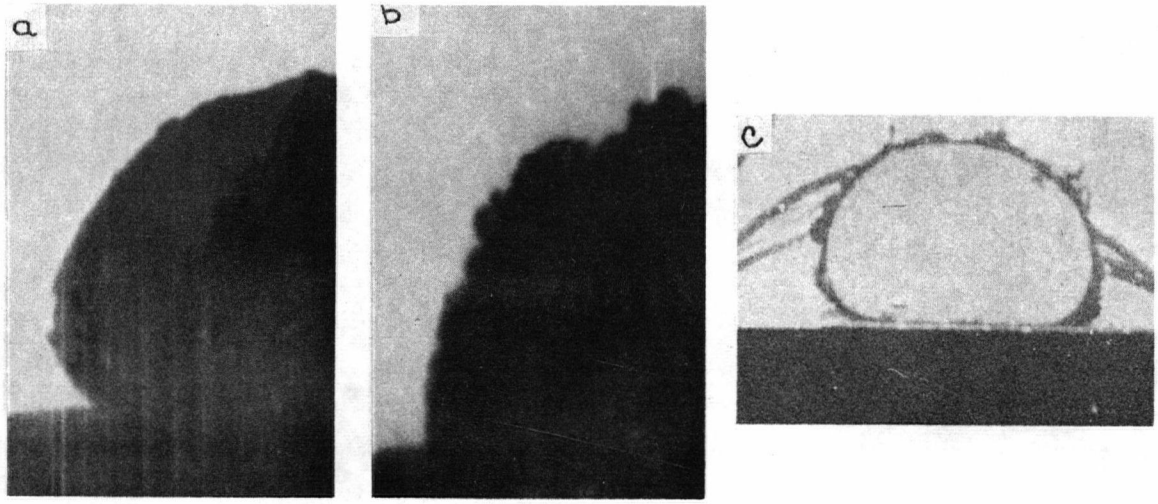

Figure 12. Effect of Sulphur on Drop Silhouette - Experiment 12

a) At melting
b) After carbon precipitation
c) Same sample sectioned to show outline of drop with respect to surface graphite.

Difficulty was also experienced in getting the sulphur into solution in the basic Fe-C alloy before vaporization of the FeS master alloy, the partial pressure of all sulphur forms over FeS at 660°C being 0.58 atmospheres[37].

No basal attack i.e., adherence of the drop to the plate, was noted for those alloys which exhibited surface graphite precipitation. This effect was used to determine whether sulphur had been dissolved into the Fe-C alloy, and γ_{LV} calculations were only made on those tests which showed no basal attack. Table IV contains the γ_{LV} values for four tests which obviously contained some sulphur. The table includes the amount of sulphur added, the per cent sulphur analysed in the drop, the contact angle, and the average properties of the Fe-C alloy. Since it was not possible to reproduce a given sulphur concentration and since sulphur contents of less than 0.01 wt.% could not be analysed the values cannot be quantitatively compared to Keverian's data. However, a decrease in γ_{LV} and an increase in ϕ with increasing sulphur is observed, consistent with Keverian's findings.

TABLE IV.

Effect of Sulphur Additions on γ_{LV} and Contact Angle.

Experiment Number	wt.% S added	wt.% S analysed	Average γ_{LV}	Equilibrium ϕ
12	1.86	0.022	338 (only an approximation)	165
36	0.30	<0.01	801	141
38	0.01	<0.01	1115	152
39	0.035	<0.01	891	145
Average Fe-C Data	-	<0.01	1152	128

4. Effect of Ce Additions

Upon melting the crucible containing the Ce alloy addition, complete solution of the addition did not occur. Instead some portion of it floated on the apex of the molten drop, its size decreasing with increasing temperature. Silhouettes from Experiment 31 are included in Figure 13 and show the effect of increasing temperature. This surface material acts as an additional force tending to flatten the drop hence changing the γ_{LV} observed.

Little change was noted in the contact angle with increasing temperatures up to 1600°C, Figure 14. Because a high angle was maintained, it was possible to determine surface tensions at the higher temperature where the extraneous surface force was minimized. The results are reported in Table V.

To check the effect of the extraneous forces a drop to which 0.04 wt.% Ce had been added was melted and the shape parameters recorded. This same drop was taken from the system, the surface deposit was removed

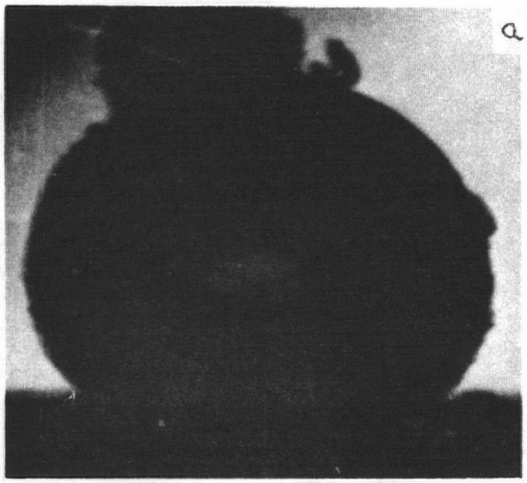

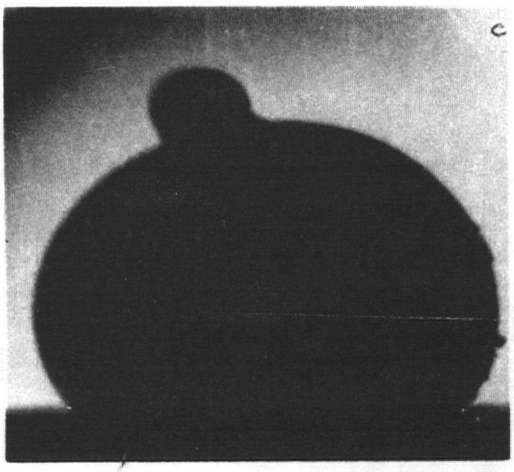

Figure 13. Silhouettes of Experiment 31, -0.05 wt.% Ce added, showing effect of temperature

a) 1285°C
b) 1305
c) 1450
d) 1615
e) 1630

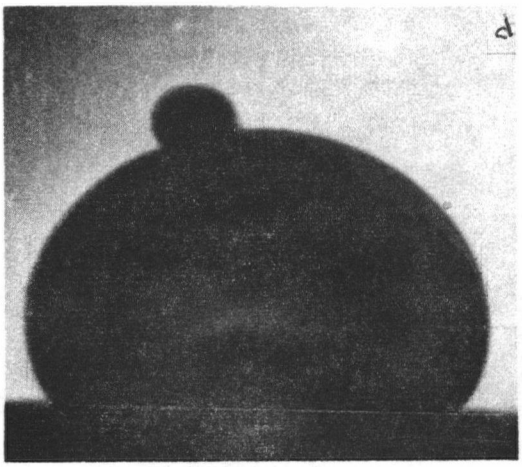

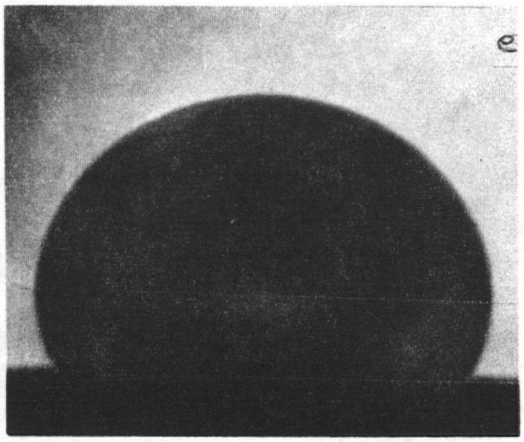

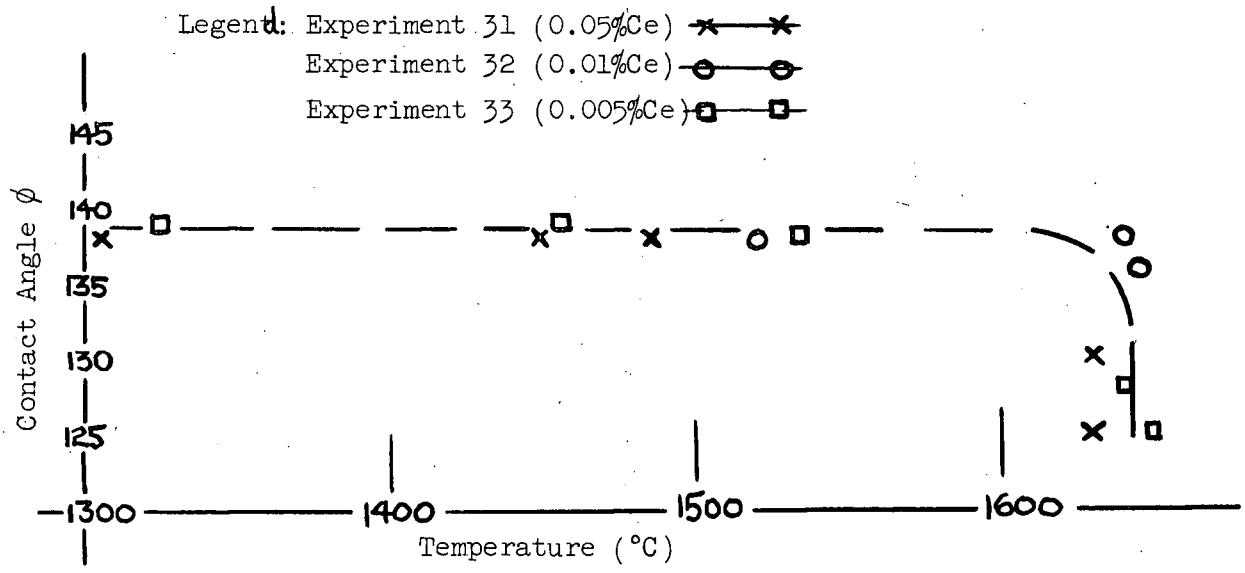

Figure 14. Contact Angle Versus Temperature for Ce Tests

TABLE V.

Effect of Ce Additions on γ_{LV} and ϕ

Exp. No.	wt.% Ce Added	wt.% Ce Analysed	Temperature Range °C	Average γ_{LV}	ϕ
30	0.05	0.05 bottom 0.02 top	1445 - 1620	611	140
31	0.025	0.05	1305 - 1630	813	138
32	0.01	<0.02	1520 - 1645	754	137
33	0.005	0.03	1315 - 1650	876	138
48	0.05	0.05	1305 - 1405	864	156
50	0.04	not analysed	1605	557	136
51	0.04	0.05 bottom 0.02 top	1600	670	139

and the test was repeated. The data obtained is included in Table V, Experiments 50 and 51. In experiment 51 a symmetrical drop shape was not obtained until a temperature of 1550°C was reached, indicating that complete remelting did not occur below this temperature.

Although the Ce data was calculated over a wide temperature range no consistent change with increasing temperature was noted.

Average interfacial energies and changes in this parameter (neglecting the temperature effect) are reported in Table VI.

TABLE VI.

Average Interfacial Energy Changes

Alloy	Average γ_{LV} (dynes/cm)	ϕ	$\gamma_{LS} - \gamma_{SV} = \gamma_{LV} \cos(180-\phi)$	Interfacial Energy Difference ✱
Fe-C	1152	128	709	basis of comparison
Fe-C-Ni	1135	118	533	- 176
Fe-C-Mn	1261	127	758	+ 49
Fe-C-S Exp. 12 (0.022%S)	≃338	165	326	- 383
Exp. 36(<0.01 wt.% S)	801	141	622	- 87
Exp. 38(<0.01 wt.% S)	1115	152	1033	+ 324
Exp. 39(<0.01 wt.% S)	891	145	730	+ 21
Fe-C-Ce				
Exp. 30 (0.05 wt.% Ce)	611	140	468	- 241
Exp. 31 (0.025 wt.% Ce)	813	138	604	- 105
Exp. 32 (0.01 wt.% Ce)	754	137	550	- 159
Exp. 33 (0.005 wt.% Ce)	876	138	650	- 59
Exp. 50 (0.04 wt.% Ce)	557	136	401	- 308
Exp. 51 (0.04 wt.% Ce)	670	136	506	- 203

✱ Neglecting temperature effects and assuming no change in γ_{SV}.

B. Results of Metallographic Examination of the Solidified Drops

1. Fe-C Alloy

A wide range of primary graphite forms persisted over the relatively small volume of the drop. The top exhibited a large amount of well developed primary graphite, while the bottom of the drop contained a compact form of primary graphite, and a much finer D-type eutectic graphite. The general structure is illustrated in Figure 15. The compact graphite does not have the smooth surface of a nodule. Instead, it resembles the center of a rosette. The primary graphite has acted as the nuclei for the eutectic graphite precipitation, explaining the large graphite-free regions surrounding the kish flakes. Plate c) shows the flakes which have developed at the interface, the base acting as the nucleating agent. These flakes are especially well developed when the drop is held at the melting temperature. The drops adhered to the base plate even when solidified from the melting temperature and the interface appeared very irregular. This would indicate that some basal attack was occurring.

To check this effect a sample was melted, held for 1/2 hour at this temperature, then allowed to solidify. Upon removing the drop from the base, small metallic crystals remained on the plate surface, as shown in Figure 16. These crystals were analyzed using powder X-ray techniques and found to be either α-iron or a mixture of α-iron and Fe_3C - the only high intensity line for Fe_3C is 2.01A°as compared to 2.02 A° for the highest intensity line of α-iron. Upon examining the drop, pearlite was present at the interface. The straight lines noted on the crystal surface were thought to be cleavage steps.

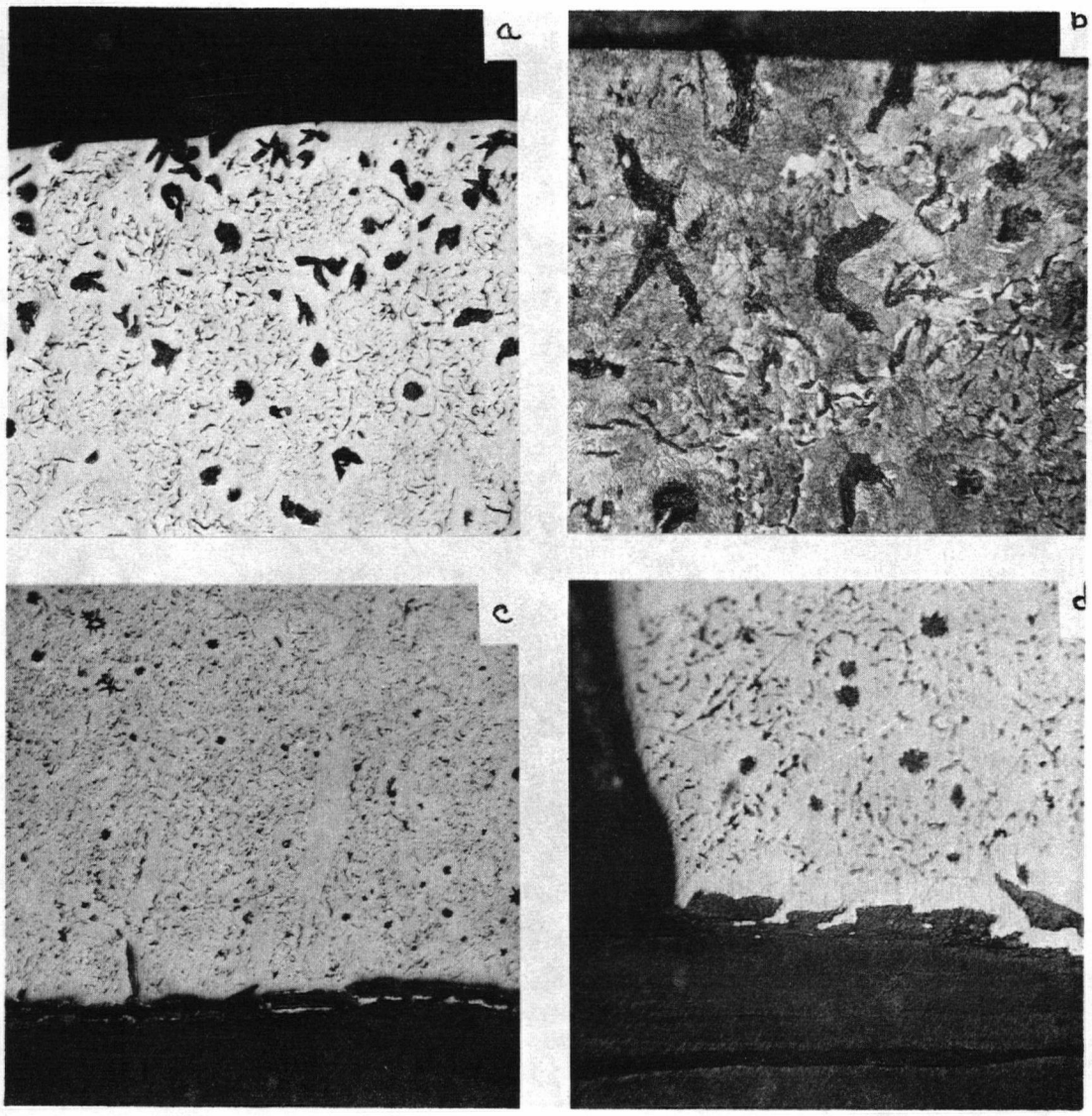

Figure 15. Fe-C Drop - Experiment 14

a) Structure near apex of drop X 150
b) Etched in Nital X 400
c) Base region of drop X 150
d) Interface Characteristics X 400

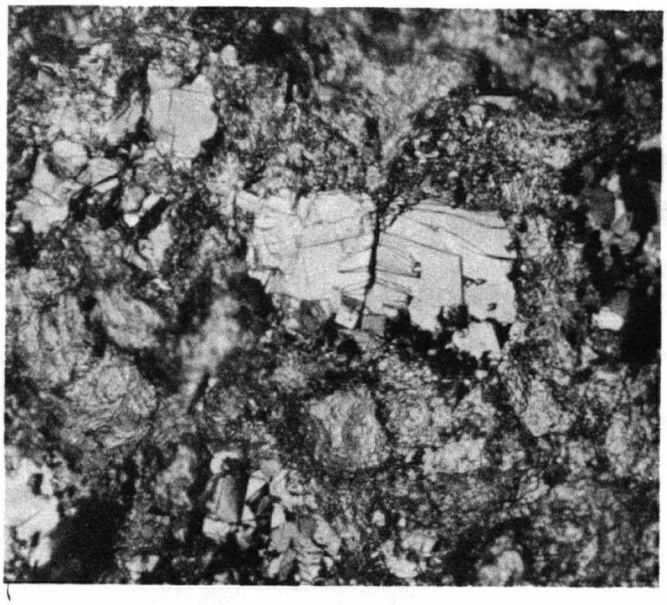

Figure 16. Metallic Crystals Remaining on Base Plate After Removal of Fe-C Drop

X 210

Some well developed primary flakes were also present at the drop interface indicative of the nucleating potential of the base and the occurrence of primary graphitization at the melting temperature.

2. Effect of Ni and Mn Additions

Figures 17 and 18 illustrate the structure of the 0.85% Ni and 1.65% Mn alloys respectively. A graphite distribution similar to that of the Fe-C alloy is noted, although the graphite is slightly coarser in both instances.

3. Effect of Sulphur Additions

The graphite form changed markedly with even small additions of sulphur. In the alloys containing 0.039% sulphur and 0.022% sulphur the graphite flakes were very large extending to the graphite covered surface with no D-type eutectic graphite being noted.

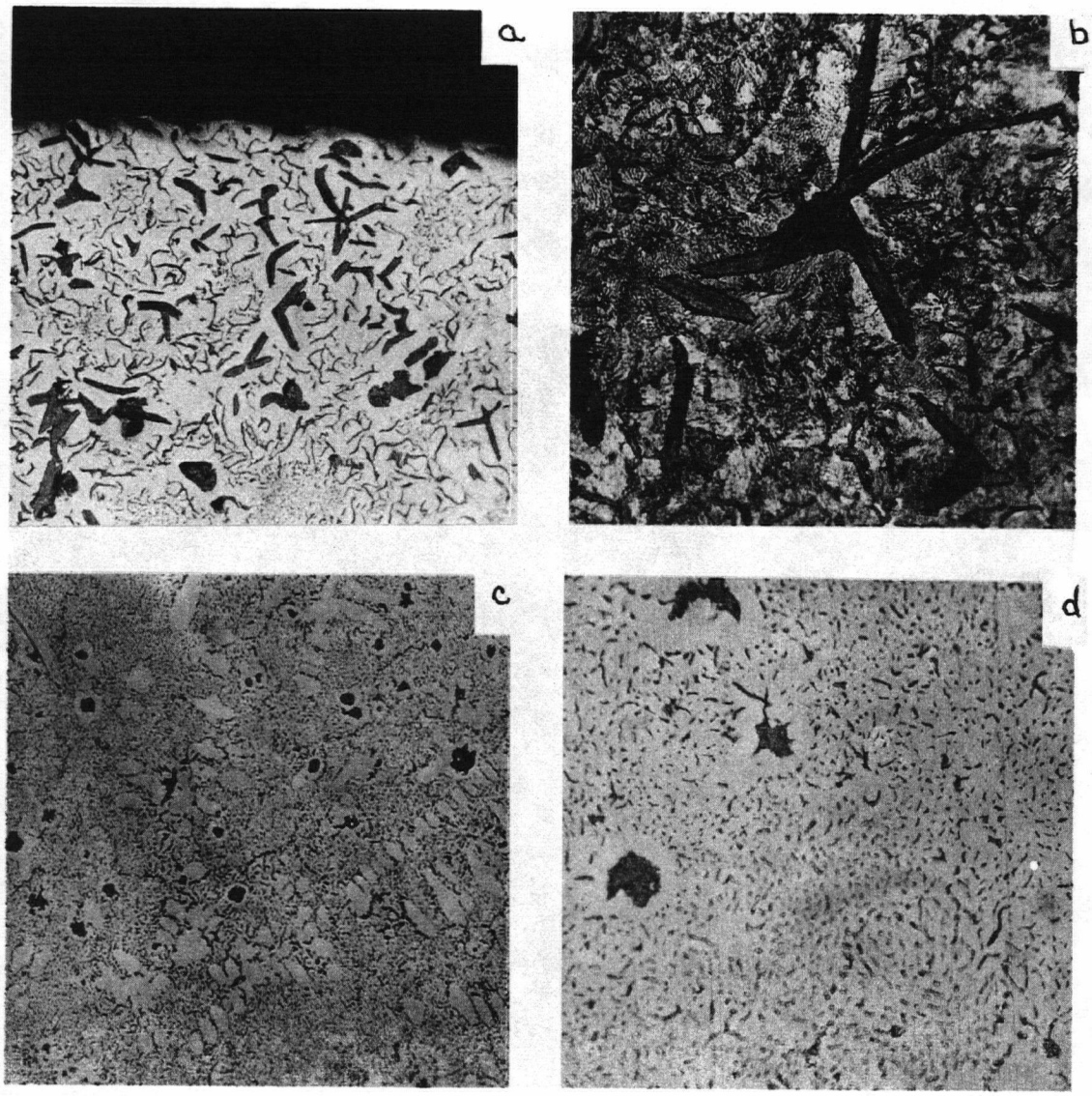

Figure 17. Structure of Drop Containing 0.85% Ni

a) Top of drop X 150
b) Etched X 400
c) Bottom region of drop X 150
e) Bottom region of drop X 400

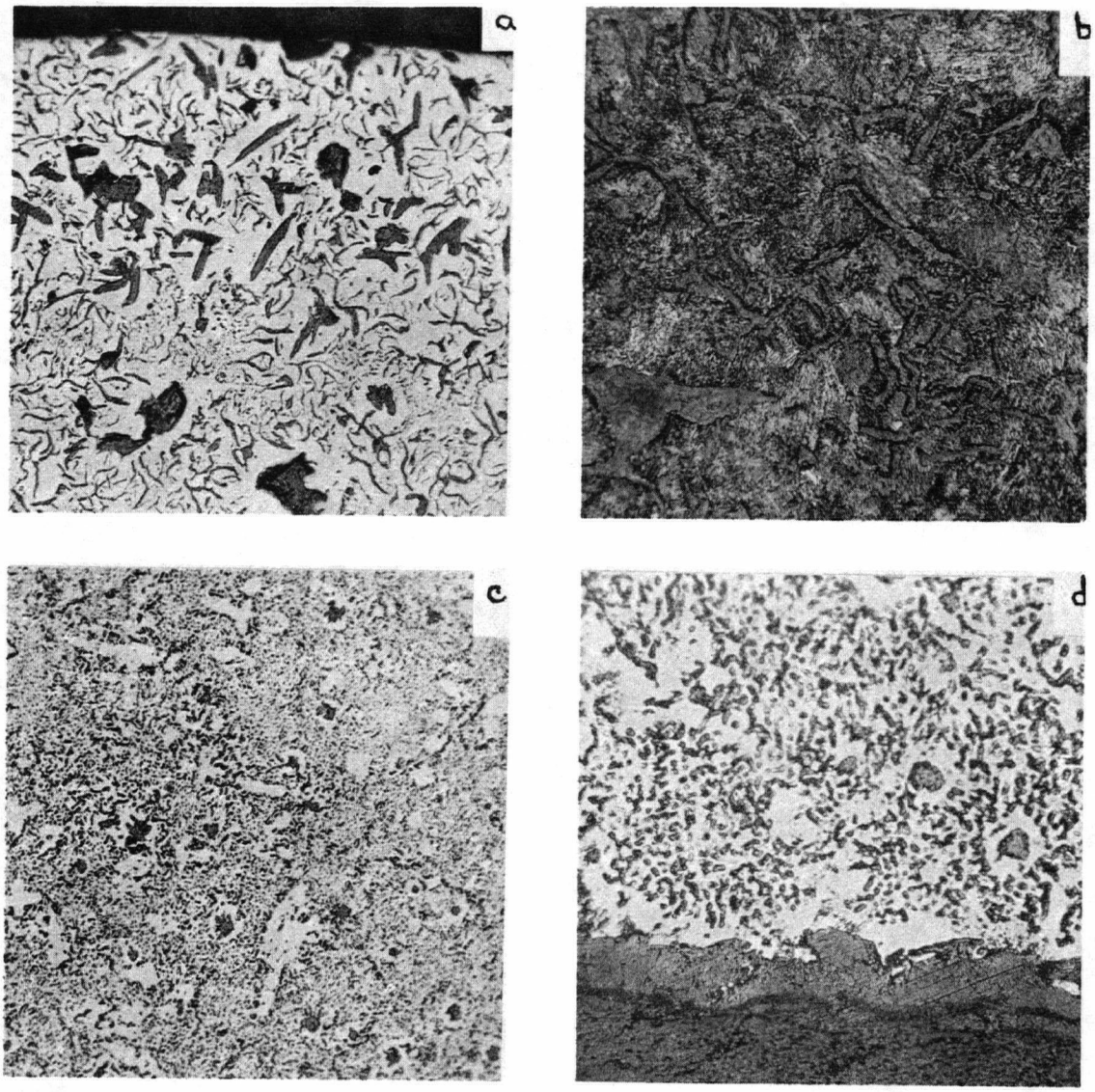

Figure 18. Structure of the 1.65% Mn Drop

a) Top of drop X 150
b) Top etched X 400
c) Bottom of drop X 150
d) Interface X 400

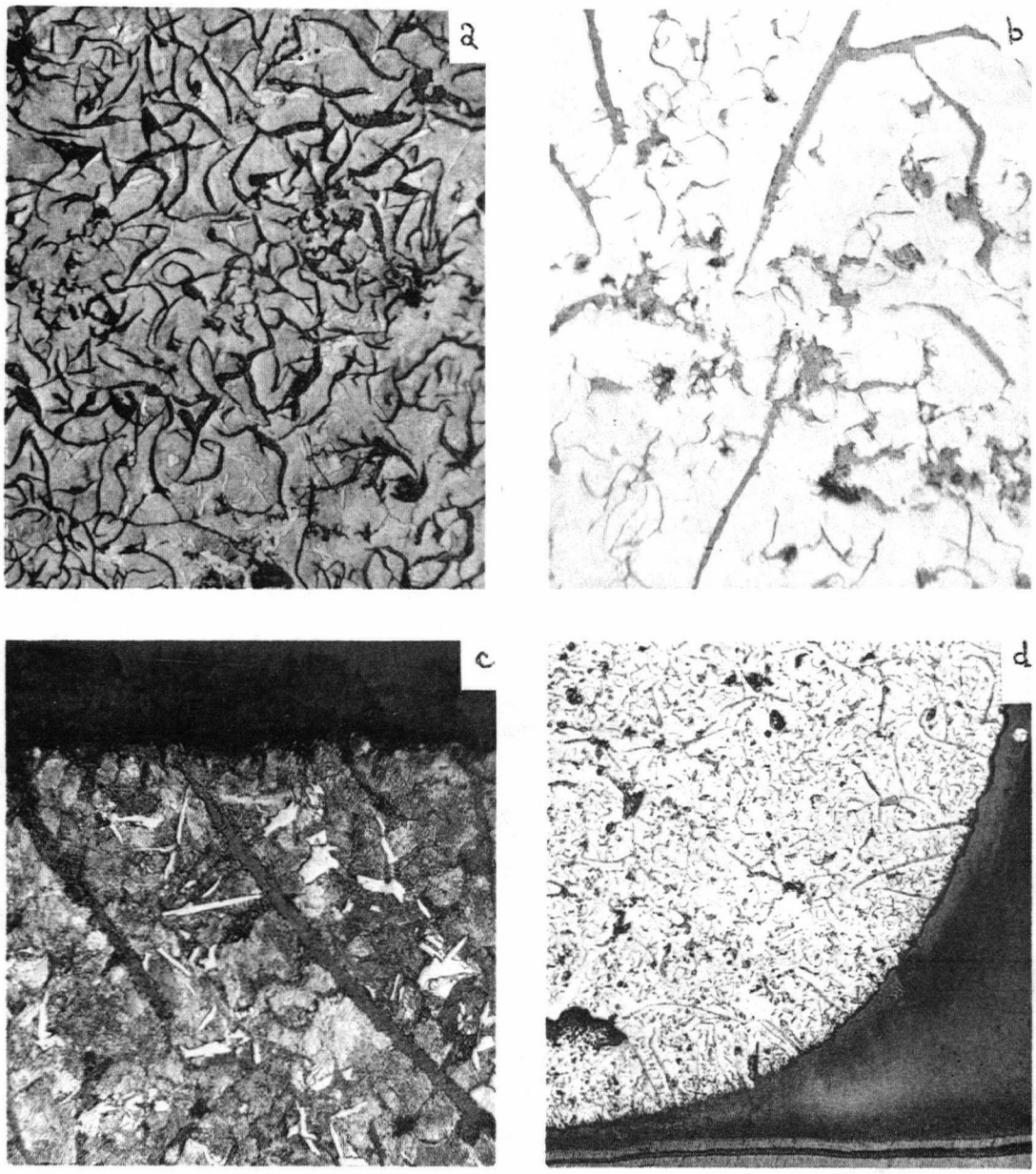

Figure 19. Structure of High Sulphur Alloys

a) 0.039% sulphur showing the large flakes, no D-type eutectic graphite and free carbide in the pearlitic matrix X 100

b) 0.022% sulphur showing the large flakes and compact graphite forms X 400

c) Top of drop b) showing the large flakes extending to the surface and free carbide in matrix X 400

d) Bottom of same drop showing the very irregular surface of the drop, the $\simeq$180° contact angle and the graphite form. X 35

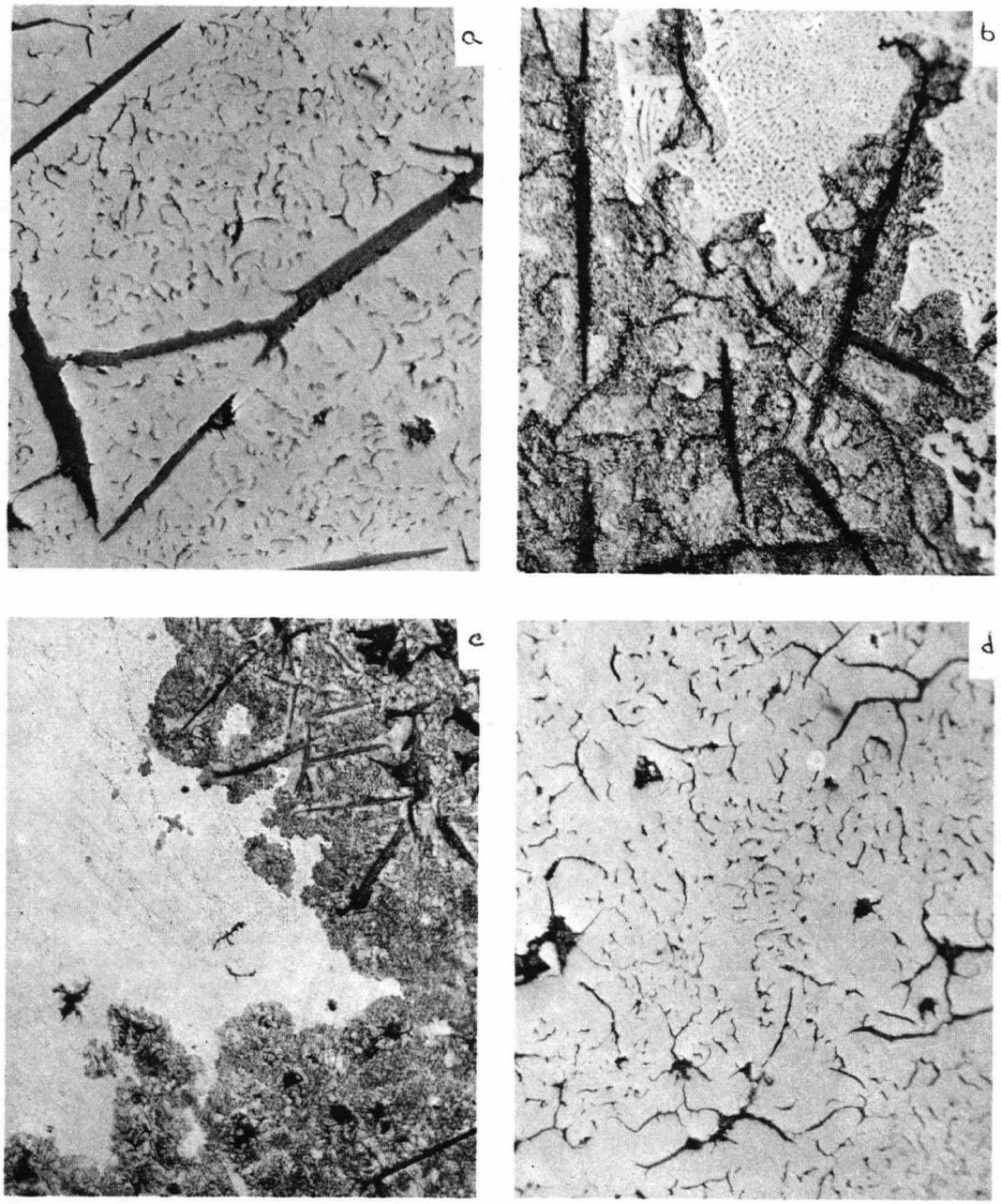

Figure 20. Structure of Alloy Containing from 0.005 to 0.01% S

a) Large flakes present near bottom of drop and D-type eutectic graphite X 400

b) Etched showing the association of the larger flakes with quenched liquid (carbide). X 400

c) Center of drop showing the flake and compact graphite, the pearlitic matrix and the central free carbide X 35

d) Bottom of drop, showing the compact graphite X 400

A compact graphite form was also present, the general structure for the two alloys being depicted in Figure 19.

Figure 20 shows the structure of an alloy containing less than 0.01 wt.% sulphur but more than the sulphur level of the basic Fe-C alloy - no wetting or adherence to the base plate being observed and the drop surface being darkened by the presence of graphite. The large flakes were again noted and were located near the base of the drop as shown in plate a) and plate b). The upper region of the drop contained a compact graphite form and D-type eutectic graphite as shown in plage c). A sharp transition existed between the flake and compact form and the massive free carbides, as depicted in plate d). The variety of graphite forms noted indicates pronounced sulphur segregation. However, the small size of the drops prohibited any analytical check.

4. Effect of Ce Additions

When Ce additions were made, the general form of the quenched drop was quite different. The surface collapsed in certain areas indicative of the greater shrinkage associated with the nodular graphite, the surface of an alloy containing 0.05 wt.% Ce being depicted in Figure 21.

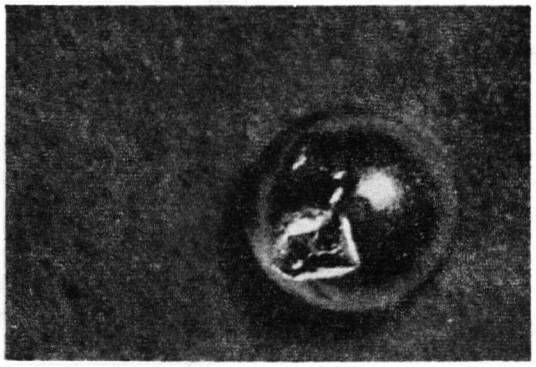

Figure 21. Collapsed Surface of Drop Containing 0.05 wt.% Ce

The small button of material apparently not soluble in the molten drop, was examined after quenching. The surface was brownish in color and upon sectioning and polishing the center was found to contain small inclusions, as shown in Figure 24 plate b). Since these did not have the same color or form as the graphite in the adjacent drop it was thought that they were sulphide inclusions, expecially since the primary action of a spheroidizing agent is the removal of sulphur as a sulphide. The sulphides being less dense would float to the top. To check this possibility the sectioned sample was placed in the electron probe and a Ce scan was conducted. Table VII shows the data obtained and comparative figures for the 0.5 wt.% Ce master alloy and the basic Fe-C alloy.

Although it was hoped that any Ce segregation within the drop could be determined by use of the probe, the small difference in the count rate between the 0.5 wt.% Ce master alloy, the Ce-free Fe-C alloy and the range of results obtained for any one position indicated that the concentration differences expected would be undetectable.

A small surface button was crushed and examined using X-ray powder techniques. Only the α lines were noted. This is explainable as the amount of material is very small and the inclusions are contained in the iron matrix.

As in the alloys previously examined, a wide range of graphite shapes persisted across the drop volume. The structure offour samples will be considered in detail as these depict the range of shapes observed.

TABLE VII.

Probe Analysis on Section of Alloy Containing 0.05 wt.% Ce

(Beam current 0.09 μa, 20 kv, Reading the Ce L_{B_1} line at 71.6°)

Position on Sample	Counts/min.	Average
Near top of drop	94, 104, 85, 70, 94, 80, 72, 64, 85, 95	84
Center of drop	84, 99, 107, 86, 98, 100, 81, 79, 75, 84	89
Near base of drop	101, 93, 85, 84, 71, 103, 96, 92, 85, 93	90
Top deposit on drop	1159, 606, 500, 800, 761	765
Fe-C Alloy (No Ce addition)	103, 90, 102, 84, 87, 92, 100, 95, 86, 89	93
Fe-C-Ce Master Alloy (0.5 wt.% Ce)	157, 140, 171, 159, 138, 161, 135, 143, 129, 150	148

Figure 22 illustrates the structure of a 0.005 wt.% Ce alloy (analysed 0.03 wt.%). Plates a) and b) show the graphite at the top of the drop, plate c) the transition from the flake through the dense rosette to the final nodular form present near the base of the drop, and plate d) the nodules and round-tipped graphite flakes present at the interface. The matrix is pearlite, showing up as white after light polishing, free carbides being distributed throughout.

Figure 23 shows the structure of a 0.04 wt.% Ce alloy (analysed average 0.02 wt.%, 0.02 on top, 0.05 on bottom). More graphite is present near the top of the drop. The star-like rosettes, plates a), b) and c), decrease in number in progressing towards the base of the drop, plate d). Some dense nodules were present at the lower boundary of the rosette forms, plates e) and f). The graphite in the lower region was sparsely distributed,

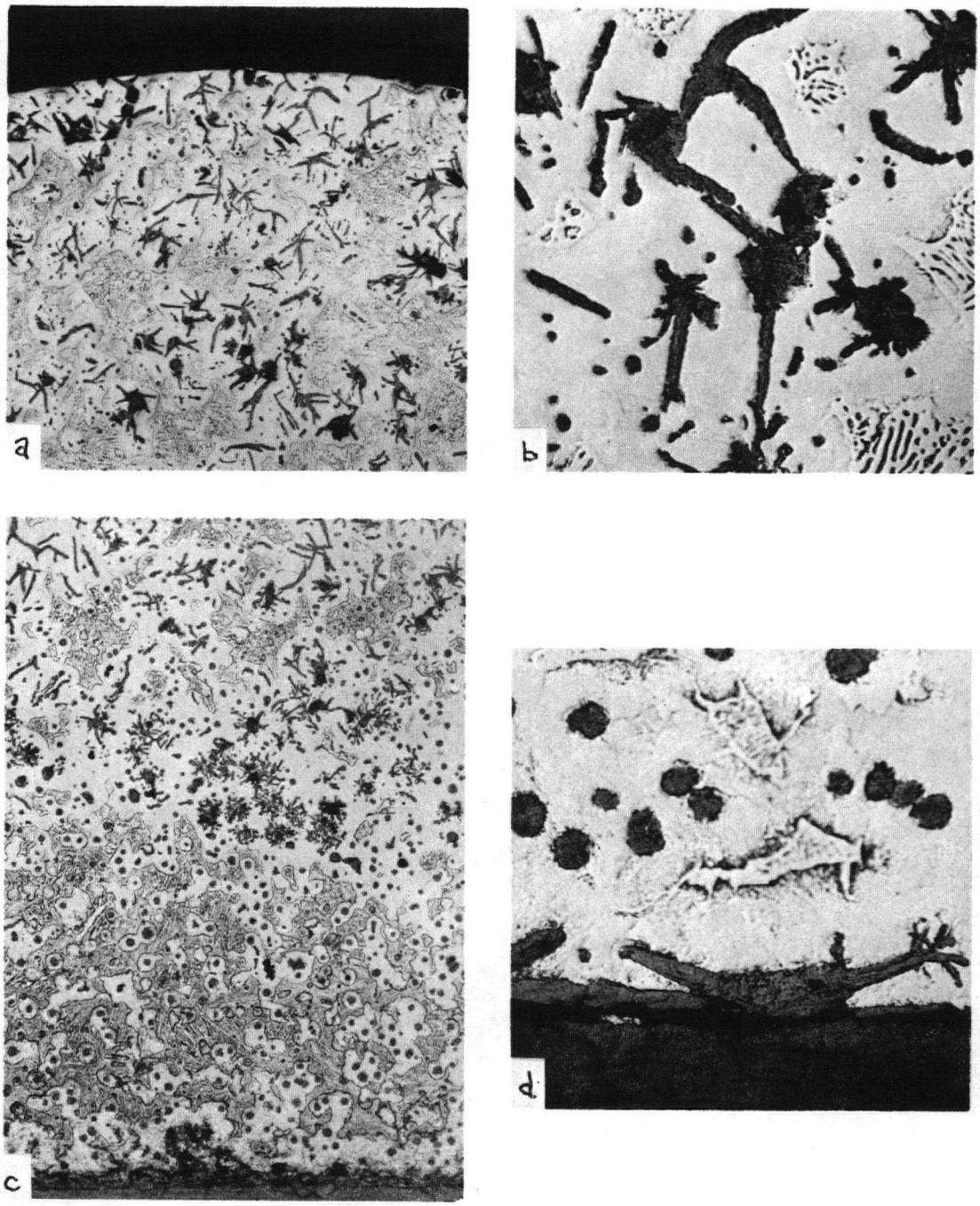

Figure 22. Graphite Structure of Experiment 33 (0.005 wt.% Ce added, analysed 0.03%).

a) Top of drop X 35 (the white intermediate region is pearlite)

b) Top of drop X 400

c) Center to bottom of drop X 35

d) Interface X 400

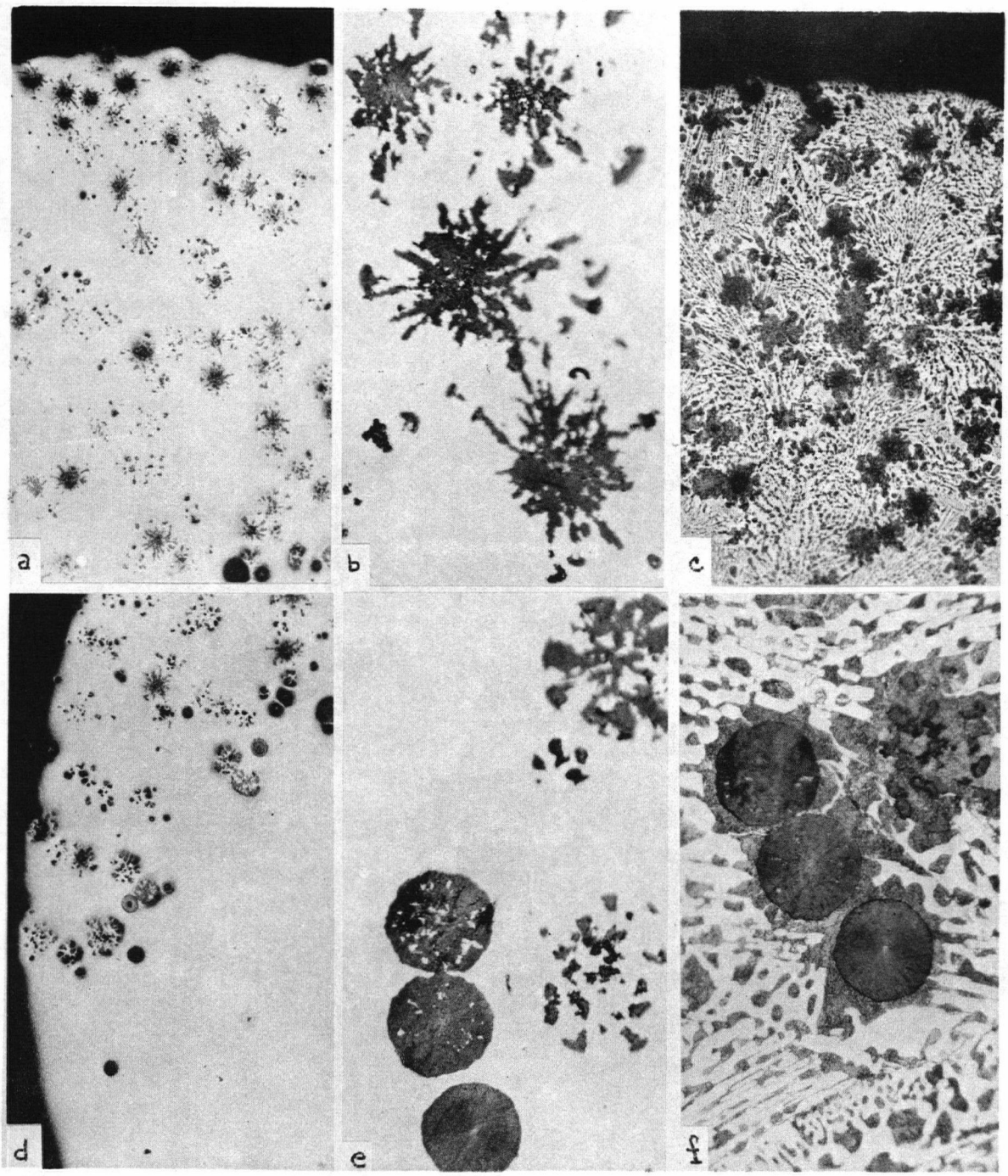

Figure 23. Structure of Alloy Containing Ce (0.04 wt.% added, analysed 0.02 top - 0.05 bottom)

a) Top of drop X 35
b) Top of drop X 400
c) Top of drop etched in 2% Nital X 35
d) Side of drop showing transition region X 35
e) Graphite in transition region X 400
f) Structure etched in Nital X 400

spheroidal in form, and surrounded by a shell of transformed austenite, plate f).

Figure 24 shows the structure of a 0.05 wt.% Ce alloy. Plate a) depicts the heavy concentration of nodules at the top of the drop. Plate b) shows the sulphide inclusions present in the undissolved material at the drop apex. Place c) and plate d) represent the graphite shapes present in the central region of the drop, with plate e) illustrating the sparsely populated base region and the layer of transformed austenite associated with the drop periphery. The graphite form contained within this layer is shown in plate f). This layer is also present in the base region of Figure 23, again accompanying the dense nodules. In Figure 24, where the nodules are poorly developed, no peripheral layer of transformed austenite is present. All three drops were quenched from approximately 1600°C and thus should have experienced the same cooling rates.

Since it was not possible to check Ce segregation in the quenched drop by the probe technique, 5 mg samples of cuttings were taken from the top and bottom of two drops and analysed spectrographically. Table VIII records the concentration differences observed.

TABLE VIII.

Ce Concentration at Top and Bottom of Drop

Experiment Number	wt.% Ce Added	wt.% Ce Analysed
30	0.05	0.02 top 0.05 bottom
51	0.04	0.02 top 0.05 bottom

Figure 24 Structure of 0.05% Ce alloy (0.05 added, analyzed 0.05, 0.02 top and 0.05 bottom)

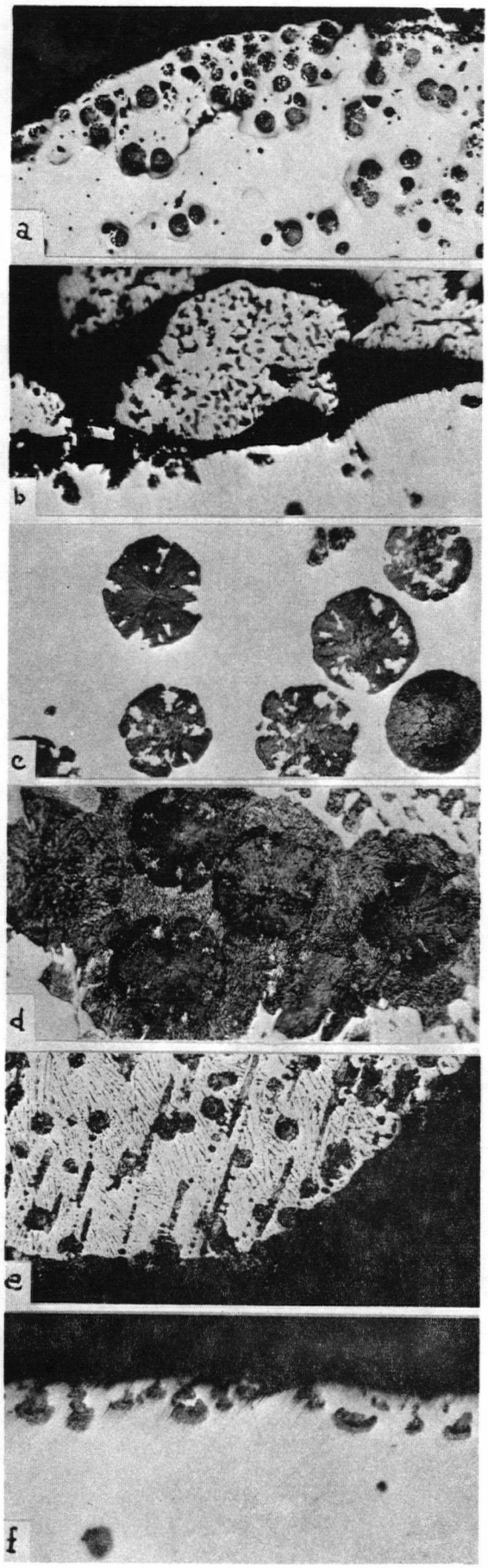

a) Top of drop X 35

b) Sulphide inclusions in surface button X 400

c) Graphite form in transition region X 400

d) Structure c) etched in Nital X 400

e) Structure of lower drop showing the compact graphite and the outer layer of transformed austenite X 150

f) Graphite in the outer layer X 400

An average final analyses of the drops is shown in Table IX.

TABLE IX.

Average Spectrographic Analyses After Test

Al	Cr	Cu	Mg	Mn	Mo	Ni	Si	Ti	V
0.0002	0.0001	0.0006	0.0002	0.0005	0.003	0.02	0.02	0.002	0.002

To permit comparison of the structural changes associated with major alloy additions, the structures of the master alloys are shown in Figure 25. The master alloys can be compared as the cooling rates are similar. The Fe-C (5.0% C) alloy is depicted in plate a), coarse primary graphite, some compact graphite, and D-type eutectic graphite being noted. The Ni alloy (10.87 %Ni, 5.2% C) is shown in plate b), a much coarser graphite flake being observed and only small regions of pearlite contained in the α matrix. The Mn (18.0% Mn, 5.25% C) alloy is illustrated in plate c). The carbide stabilizing power of the Mn is evident when examining this structure. The Ce master alloy (0.53 % Ce, 5.7% C) is shown in plate d). Several large, dense nodules have developed. However, in general the nodules are very small and well distributed throughout the carbide matrix. Some carbon deposition on the small nodules has occurred as a shell of transformed austenite surrounds each nodule. These cannot be considered as nuclei for this reason.

The sulphur master alloy is not included as it was a eutectic mixture of FeS and FeS_2 and hence contained no free graphite.

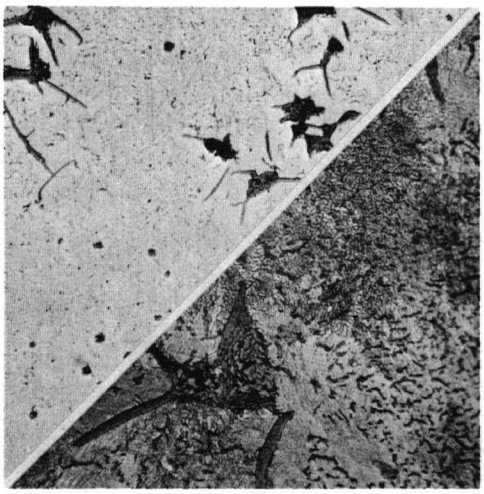

Figure 25. Structure of Master Alloys

a) Fe-C master alloy structure

X 150

X 400 etched in Nital

b) Fe-C-Ni (10.87% Ni)
Unetched and
Etched X 200

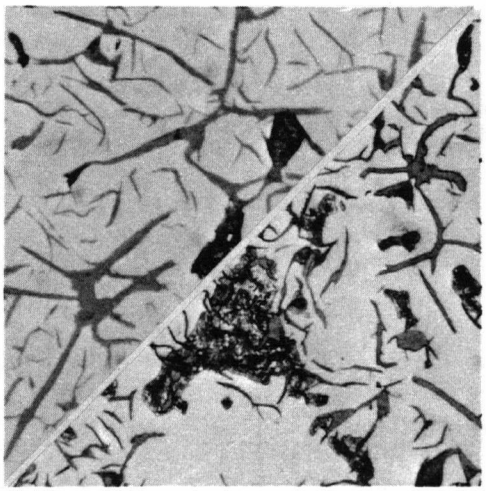

c) Fe-C-Mn (18% Mn) Etched X 110

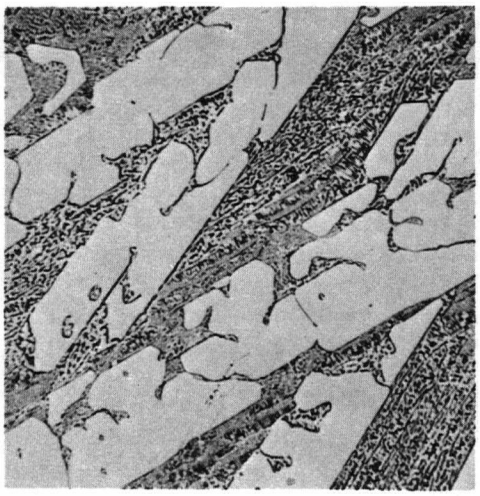

d) Fe-C-Ce
Unetched and
Etched X 110

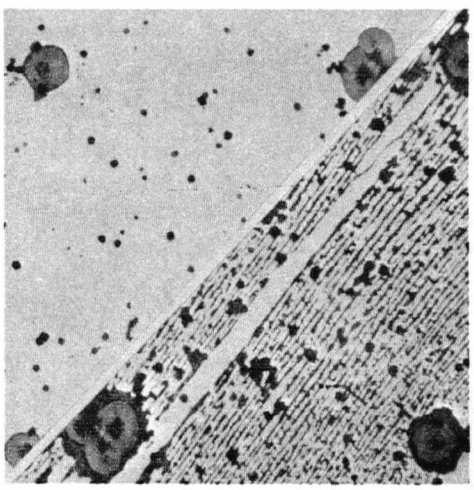

C. Thermodynamic Calculations

Because the surface tension of the Fe-C alloys is markedly affected by oxygen contamination, it was necessary to determine the per cent oxygen expected in the melt under the conditions employed. Elliott[40] has examined the equilibrium reaction

$$[C]_{Fe} + [O]_{\text{in Fe}} \rightleftharpoons CO_{(gas)}$$

and has shown that the equilibrium oxygen content at 1600°C is approximately 0.0065% at carbon saturation at 1 atmosphere pressure (essentially CO). This was determined from the reaction:

$$1/2\ O_2 \rightleftharpoons [O]_{\%\text{ in Fe}}$$

$\Delta F^\circ = -27{,}930 - 0.57\ T = -28{,}998$ (at 1600°C).

The oxygen partial pressure was determined from

$-\log P_{O_2}$ at 1 atmosphere total pressure = 15.2[40]

$$\therefore\ P_{O_2} = 6.3 \times 10^{-16}$$

From $\Delta F^\circ = -RT \ln \dfrac{[O]_{\%\text{ of Fe}}}{[P_{O_2}]^{1/2}}$

$$[O]_{\%\text{ in Fe}} = 0.00006$$

Correcting this using the activity coefficient of oxygen in carbon saturated iron at 1600°C

$$\text{i.e.,}\quad \log f_O^{(C)} = 1 \times 10^{-2}$$

$$\therefore\ \%\ O \text{ in Fe} = \frac{a_O}{f} = 0.006 \text{ wt. } \%$$

Repeating this calculation for a lower pressure, i.e., 0.01 atm. CO

$-\log P_{O_2}$ at carbon saturation is approximately 19 from

extrapolation of Elliott's data

$$\therefore \quad \log [O]_{\% \text{ in Fe}} = -6.12$$

and using $f_O^{(c)} = 10^{-2}$, % O in carbon saturated iron =

$$10^{-4.12} = 7.6 \times 10^{-5}$$

In the system in this thesis the pressure was maintained at 10^{-5} mm or 10^{-8} atmospheres. The equilibrium concentration of oxygen in the melt would thus be expected to be very low.

The partial pressure of oxygen associated with molybdenum oxide was calculated as follows:

$$MoO_{2(s)} \rightleftharpoons Mo_{(s)} + O_{2(gas)} \quad [41]$$

$$\Delta F^\circ = 137{,}000 - 39.4\ T$$

$$\text{at } 1600^\circ C = 63{,}200$$

$$\therefore \quad P_{O_2} = 4.17 \times 10^{-8} \text{ atmospheres}$$

Since some FeO may be introduced to the system the associated partial pressure of oxygen was also determined.

$$FeO_{(l)} \rightleftharpoons Fe_{(l)} + 1/2\ O_{2(gas)} \quad [41]$$

$$\Delta F^\circ = 56{,}830 - 11.94\ T$$

$$\text{at } 1600^\circ C = 34{,}430$$

$$\therefore \quad P_{O_2} = 8.3 \times 10^{-9} \text{ atmospheres.}$$

Since it is believed that CeS is formed with Ce additions to the Fe-C alloy the thermodynamics of this reaction was checked. The reaction of interest is:

$$C_{(\% \text{ in C saturated Fe})} + S_{(\% \text{ in C saturated Fe})} \rightleftharpoons CeS_{(\text{pure})}$$

The following free energy equations have been used:

a) $Ce_s + 1/2\ S_{2\ g} \rightleftharpoons CeS_s$ [39]

$\Delta F^\circ_a = -133,400 + 20T$

b) $Ce_s \rightleftharpoons Ce_l$ [39]

$\Delta F^\circ_b = 2200 - 2.0\ T$

c) $Ce_l \rightleftharpoons Ce_{(\%\ in\ Fe)}$

Assuming an ideal solution for lack of appropriate data

$$\Delta F^\circ_c = RT \ln \frac{0.5585}{140.13} = -11(.0\ T$$

d) $1/2\ S_{2\ g} \rightleftharpoons S_{(\%\ in\ Fe)}$

$\Delta F^\circ_d = -31,520 + 5.27\ T$ [39]

ΔF° for the formation of cerium sulphide from the elements in an iron melt = $\Delta F^\circ_a - \Delta F^\circ_b - \Delta F^\circ_c - \Delta F^\circ_d = -104,080 + 27.7\ T$

Thus in an iron alloy at 1800°K (1527°C) $\Delta F^\circ = -54,080$ cal. and log K = 6.57. If solid CeS is present, $[\%Ce][\%S] = 10^{-6.57}$. Thus in an iron alloy in which excess Ce (beyond that required to form CeS) is present, the final S activity will be extremely low. For example, in a liquid iron containing 0.005% S and 0.05% Ce, the excess Ce concentration will be approximately 0.03%. If, as already assumed, Ce forms an ideal solution with iron, the equilibrium S activity (1% standard state), will be $10^{-5.05}$.

The effect of C saturation on the activity coefficient of Ce in dilute solution in liquid iron is not known and therefore ideality must be assumed. Under the same conditions of C saturation log f_s is about 0.7 and the equilibrium S concentration in the alloy will be of the order of 10^{-6}%.

IV. DISCUSSION AND CONCLUSIONS

The wide range of γ_{LV} values obtained in any one test is indicative of the errors inherent in the experimental approach and includes the apparatus limitations and the action of extraneous forces which distort the drop form. The greatest single error is probably realized in measuring the z parameter. Table III shows that a variation of ± 0.01" in this parameter can account for a γ_{LV} change of ± 130 dynes/cm, this being approximately the same as the calculated standard deviation.

Such a measurement limitation could arise from a lack of sharpness in the original negative, this error being magnified in obtaining the desired images. It is possible that electrically induced oscillations, mechanical vibrations or movements related to the spreading action could contribute to this effect. In addition any movements from the original position would also change the magnification. The drop shape could also be distorted by an extraneous force or unsymmetrical wetting action. There is also an inherent difficulty involved in obtaining the z parameter.

Because the Fe-C drops are bonded to the base plate after cooling from the melting temperature and because the resulting interface is quite irregular the possibility of a reaction at this interface arises. This would also affect the reproducibility of the results and require an explanation as the Fe-C alloys were initially carbon saturated.

The structure of the alloys indicated that primary graphitization occurred at the melting temperature, localized, large flakes developing at the interface. The upper region in the drop contained a heavier, more developed primary graphite. This was related to a lower cooling rate and a floating of primary graphite from the basal region.

Under "equilibrium" conditions a flux of carbon atoms is being transferred between the graphite and the melt. Since in the lower areas of the drop little primary graphite is present, a flux between the melt and the base plate results. This would account for the interface reaction even though the Fe-C alloy was initially carbon saturated. Because this reaction does not seriously alter the drop shape and because no additional compounds are formed, the sessile drop approach is still valid.

The average γ_{LV} for the Fe-C alloys is in qualitative agreement with Kozakevitch's data[15] which predicts a value of 1100 to 1200 dynes/cm for a sulphur content of approximately 0.005 wt.%, 4.5 wt.% C and a temperature of 1450°C. However, the sensitivity limitation in the S analyses (i.e., values $<$ 0.01% could not be determined) precludes a quantitative comparison.

The average contact angle of 128° for 1290 to 1335°C compares favorably with a value of 121° found in Keverian's work[2], the difference being attributable to the lower S content of his alloys (0.0005%) and his use of a randomly oriented graphite surface.

Small additions of Ni did not significantly change the surface energy characteristics in agreement with the data reported by Kaufman and Whalen[17] for a 1.5% C alloy. This would indicate that no atomic interactions occur between the Ni and C atoms.

No changes were noted with manganese additions up to 1.65wt.%.

It is not possible to place any emphasis on the sulphur data due to its poor reproducibility. However, the general decrease in γ_{LV}

and increase in contact angle with sulphur additions is in agreement with Keverian's data[2] and the structural changes are similar to those reported by Garber[26] and Williams[27].

It is generally believed that the graphite-melt interfacial energy is reduced with sulphur additions. In this work it was observed that the presence of sulphur caused excess carbon to be precipitated at the drop surface, although it was expected that it would precipitate onto the primary graphite already present within the drop. This may indicate an increase in the graphite-melt interfacial energy. However, the surface energy data was insufficient to test this hypothesis.

The addition of Ce to the Fe-C alloy apparently decreased the γ_{LV} as predicted by Minkoff[18]. However, the γ_{LV} values were obtained at a higher temperature than the Fe-C γ_{LV} values. Since it was not possible to determine the temperature effect, a true comparison of the values cannot be made. Although specific values cannot therefore be assigned to the interfacial energy differences this difference was noted to increase with increasing Ce content. Such a change indicates that Ce is being adsorbed to the graphite-melt interface, a negative change in $\partial\gamma$ implying a positive change in Γ_2 from:

$$-\frac{C_2}{RT}\frac{\partial\gamma_{SL}}{\partial C_2} = \Gamma_2$$

The importance of Ce in obtaining the nodular form has been established. The nodules are only well developed in the lower region of the drop where the Ce content is the highest. It is possible that a flux of Ce atoms is required to ensure the development of the nodule, this Ce being adsorbed onto the graphite surface.

Although the inclusions noted in the "button" remaining on the drop surface could be CeS, the amount observed does not seem consistent with the very low S content of the alloy. In addition, the top and the bottom Ce analyses indicated that Ce was only removed from the top of the drop. Since a Ce depletion of in excess of four times the weight of sulphur is required to form CeS then sulphur was also only removed from this region, further decreasing the possible volume of CeS.

As an alternative explanation these inclusions could be related to the small graphite nodules present in the Ce master alloy. The fact that the Ce content is extremely high in this region would imply that Ce has been preferentially adsorbed on the inclusions. This would be consistent with the data previously considered. These inclusions are much closer packed in the "button" than are the nodules in the master alloy. Hence a higher Ce content would be expected. It was not possible to differentiate between these two theories as the volume of the inclusions was very small making X-ray analysis unsuccessful.

It has been found that the marked change in the graphite form in progressing from the top to the bottom of the Fe-C-Ce drops is associated with a change in the Ce content. The structure of the other alloys indicates that the variation is primarily related to either a high rate of cooling in the interface region or a decrease in the nucleating potential of this region resulting in supercooling. Cooling rate considerations are contained in Appendix V. Although it is not possible to establish the lines of heat flow it is apparent that a higher rate of cooling in the interface region is quite possible.

Such considerations must also apply to the Ce alloys. If it is accepted that a nodule has a surrounding shell of austenite above the eutectic temperature then the nucleating surface for austenite is already present and hence no eutectic supercooling would be expected. However as fewer nodules are present in the basal region it is likely the combinations of effects which leads to the finer structures observed.

The contact angle in the Ce tests did not change from 1300 to 1600°C. In the development of a nodule the graphite is surrounded by a shell of austenite. If the experimental analogy is complete then the base plate-melt interface is analgous to the nodule-melt interface and hence an austenite layer should develop. Because this is a solid shell little effect from increasing the temperature would be expected. However, if the main justification for the presence of the austenitic shell is the requirement that an average carbon content be maintained then a layer of austenite at the interface would not be expected.

In progressing from the flake to the nodular form only small changes in the interfacial energy were noted. The shape was more dependent on the Ce content and the position within the drop i.e., the cooling rate and carbon deposition characteristics.

It is important to note that transition stages exist in changing from the flake to the nodular form. This would imply that it is not simply a nucleation problem but is also dependent on the solidification conditions. The fact that the flakes first become rounded at the tips is generally associated with a point diffusion effect. The second stage is a compact rosette shape, this being a further increase in the surrounding area per

unit volume of precipitate. The final nodular form has a maximum sphere of influence. Such a transition does not require a spheroidal nuclei. Rather, with increase in the cooling rate in progressing towards the base of the drop, the diffusion distance of the precipitating carbon is decreased, a greater sphere of influence and hence greater surface per unit volume resulting to permit the carbon deposition.

In general the data indicates that the final graphite form is more dependent on the growth conditions than on the interfacial energies. The interfacial energy is probably only of major importance when dealing with the nucleating shape, the final form being a result of the rates of deposition on the various crystal faces.

V. RECOMMENDATIONS FOR FUTURE WORK

A similar investigation using iron of a much higher purity and master alloys having the desired compositions would eliminate several of the difficulties experienced in this work. If drops of approximately two grams were used the reproducibility would be much improved. The inclusion of facilities permitting the degassing of the base plate prior to the test would also aid in this respect.

Although the sessile drop technique can yield valuable information a more fruitful approach would be to study the growth kinetics and the development morphology of the various graphite forms. Information of this nature is required before shape transformations can be completely understood.

VI. APPENDICES

APPENDIX I.

Experimental Difficulties and Errors Inherent in the Sessile Drop Approach

Although the sessile drop technique seems simple, many hazards befall the unwary. To impart some appreciation for these difficulties several of the experimental problems will be briefly discussed[4].

1. Sample Contamination

Sample contamination is probably the most important single factor. Special care must be taken to eliminate any contaminating source. Where oxidation is a problem, as with iron, it is necessary to eliminate oxygen from the system and to remove, if possible, any oxide contamination from the material being melted. Use of a titanium or molybdenum susceptor although the latter is less effective, aids in reducing the oxygen partial pressure in an induction unit. To ensure that no oxide contamination is present it may be necessary to resort to use of an inert atmosphere. However, since the values obtained are only representative of the conditions employed, information from such experiments may be less useful. Some problems may also arise from contamination of the plate surface by the inert gas.

If possible, it is recommended that the base plate and apparatus be degassed at a high vacuum and at a temperature above that to be used. This requires that the sample be transportable to the heating section following the degassing operation.

To prevent contamination it is also necessary to trap out diffusion pumps and any source of oil or grease.

2. Problems Inherent in the Drop Shape Approach

The drop sample will be in a state of equilibrium only when its vapour pressure is less than that of the system. However, when the equilibrium vapour pressure of the melt is greater than the vacuum maintained by the system, the metal will continuously vaporize. Although such a condition cannot be considered an equilibrium condition, only a slight change in drop dimensions should result. If the equilibrium pressure were similar to the vacuum maintained this would not be a serious problem.

As in any wetting experiment, much emphasis is placed on the condition of the surface and on the possibility of variation in the contact angle when dealing with an advancing as opposed to a receding interface. Bartell and Wooley[42] have shown that for an advancing interface the contact angle depends on the previous surface treatment, whereas for a receding interface the angle is dependent on the characteristics of the wetted surface, both being correct angles for the specific conditions involved.

The possibility that the contact angle may vary around the drop also arises. This affect can be reduced by taking several measurements around the drop.

The accuracy of the technique is also dependent on the volume of the drop, this being a function of x/z. Baes and Backs[43] have shown that an optimum range for x/z is 1.15 to 1.7

The greatest difficulty in obtaining the desired parameters is experienced in determining the distance from the maximum drop diameter to the apex, i.e., the distance z. This is especially true for small drops having a high surface tension since the shape approaches that of a sphere, and for drops having a contact angle approaching 90°. Bashforth[34] has included a technique where by using successive approximations an accurate determination of this parameter can be made. However, many mathematical manipulations are necessary before this is a workable solution.

3. Equipment Design

Any errors in the optical system used to record the drop shape will result in poor reproducibility. This effect can be minimized by avoiding the need for enlargement of the image.

Any uncertainty in the magnification will markedly affect the reproducibility since the square of this parameter is inversely proportional to γ_{LV}.

Image distortions may arise due to temperature induced refraction effects. The magnitude of this effect can be determined by photographing an object of known size under identical temperature and pressure conditions. Considering the difficulties involved it is certainly to the credit of those investigators who are able to obtain reproducible results.

APPENDIX II.

Production and Properties of Pyrolytic Graphite

Pyrolytic graphite[36, 44, 45] like that employed for the base plate is produced by cracking a hydrocarbon gas onto a flat surface maintained at approximately 2000°C. The resulting dense deposit is composed of carbon atoms arranged in two dimensional hexagonal networks aligned parallel to the deposition plane. Adjacent layers exhibit random orientations preventing the material from having the three dimensional characteristics of a graphite single crystal. This crystal anisotropy is transferred to the bulk properties of the material, a high electrical and thermal conductivity being observed for directions parallel to the basal plane whereas the material behaves as an insulator in the direction perpendicular to the plane.

The macrostructure of a deposit is determined by the roughness of the precipitating surface. Growth nucleates at specific locales, a radial type of development ensuing. The end result is the conical growth visible under polarized light, the structure of the material used being shown in Figure 26. The surface of the material has a "pimpled" texture as a result of this development.

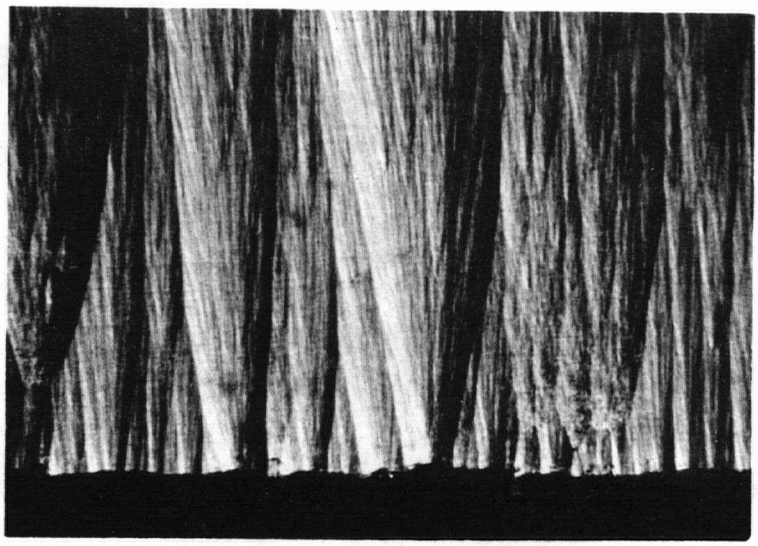

Figure 26. Section Through the Pyrolytic Graphite.
Polarized light

X 100

APPENDIX III.

Sessile Drop Data

Time After Start of Melting	Mag. of Photo	Temp. °C	x	z	x^1	z^1	δ_{LV}	ϕ
			(inches)				(dynes/cm)	
Fe-C Alloy								
Experiment No. 14								
at melting	12.88	1325	1.232	1.125	0.893	1.870	791	145
+ 1 sec.			1.230	1.150	0.917	1.860	1126	140
+ 2			1.235	1.155			1134	
+ 3			1.240	1.165			1164	
+ 4			1.235	1.170			1438	
+ 5			1.242	1.173	0.937	1.865	1379	138
+ 6			1.242	1.163			1060	
+ 7			1.240	1.155			1076	
+ 8			1.240	1.150			909	
+ 9			1.247	1.160	0.945	1.863	1103	139
+ 10			1.250	1.160			1034	
+ 11			1.257	1.153			916	
+ 12			1.247	1.170			1248	
+ 13			1.240	1.160			1164	
+ 14			1.247	1.175	0.972	1.848	1364	135
+ 15			1.244	1.165			1164	
+ 16			1.247	1.170			1295	
+ 17			1.241	1.150			897	
+ 18			1.257	1.180			1318	
+ 19			1.261	1.175			1144	
+ 20			1.256	1.172			1174	
+ 21			1.262	1.183	1.007	1.840	1242	133
+ 22			1.250	1.170			1184	
+ 23			1.250	1.150			909	
+ 24			1.250	1.170			1184	
+ 25			1.260	1.163	1.005	1.837	1006	
+ 26			1.260	1.180			1199	
+ 27			1.257	1.185	1.015	1.815	1405	132
2 min.25 sec.			1.257	1.169	1.073	1.696	1126	127
4 min.10 sec.		1335	1.257	1.183	1.068	1.708	1354	126
Experiment No. 19								
at start	11.40	1325	1.030	0.940			721	
+ 1 sec.			1.035	0.965	0.685	1.635	979	150
+ 2			1.030	0.965			1032	
+ 3			1.030	0.960			970	
+ 4			1.032	0.970	0.702	1.640	1123	148
+ 5			1.034	0.965			989	
+ 6			1.032	0.970			1120	
+ 7			1.035	0.970			1070	

continued...

Time After Start of Melting	Mag. of Photo	Temp. °C	x	z	x^1	z^1	γ_{LV}	∅
				(inches)			(dynes/cm)	
+ 8 sec.	11.40	1325	1.032	0.980	0.695	1.632	1370	146
+ 9			1.032	0.930			1370	
+ 10			1.032	0.965			1031	
+ 11			1.035	0.970			1071	
+ 12			1.035	0.965			979	
+ 13			1.035	0.971			1072	
+ 14			1.035	0.965			994	
+ 15			1.035	0.975			1170	
+ 16			1.032	0.970			1122	
+ 17			1.035	0.970			1039	
+ 18			1.040	0.970			1006	
+ 19			1.035	0.975	0.707	1.630	1167	146
+ 20			1.032	0.965			1033	
+ 21			1.040	0.965			922	
+ 22			1.035	0.965	0.720	1.620	979	145
+ 23			1.037	0.978			1213	
+ 24			1.033	0.960	0.740	1.695	941	144
2 min. 12 sec.			1.035	0.967	0.813	1.070	1024	135
3 min. 48 sec.			1.037	0.975	0.861	1.063	1150	129
Experiment No. 20 (Melting conducted on nucleating surface of plate)								
+ 16 sec.	10.35	1280	1.053	0.975	0.715	1.695	1262	150
+ 17			1.068	0.975			964	
+ 18			1.062	0.988			1231	
+ 19			1.065	0.993			1282	
+ 20			1.065	0.980	0.712	1.675	1052	151
+ 21			1.070	0.970			889	
+ 22			1.060	0.985			1210	
+ 23			1.067	0.977			1002	
+ 24			1.067	0.975	0.710	1.675	971	152
+ 25			1.065	0.973			968	
+ 26			1.062	0.988			1231	
+ 27			1.065	0.975			993	
+ 28			1.062	0.983	0.715	1.675	1044	149
+ 29			1.065	0.990			1212	
+ 30			1.065	0.985			1140	
+ 31			1.069	0.980			1014	
+ 32			1.065	0.978	0.694	1.675	1031	152
+ 33			1.067	0.980			1033	
+ 34			1.065	0.977			1021	
+ 35			1.070	0.973	0.725	1.670	917	151
+ 42			1.055	0.955	0.730	1.605	917	149
3 min.			1.050	0.967	0.735	1.585	1098	148
3 min. 2 sec.			1.050	0.970	0.735	1.582	1151	147
4 min.			1.050	0.954	0.752	1.570	934	147
4 min. 1 sec.			1.047	0.960	0.752	1.575	1070	145
5 min.			1.052	0.962	0.760	1.570	1085	145
5 min. 1 sec.			1.050	0.965	0.757	1.575	1071	144
9 min.			1.050	0.957	0.795	1.535	964	141
9 min. 1 sec.			1.052	0.965	0.800	1.550	1036	140
10 min. 24 sec.		1330	1.055	0.965	0.840	1.520	1019	136

continued...

Time After Start of Melting	Mag. of Photo	Temp. °C	x	z (inches)	x^1	z^1	γ_{LV} (dynes/cm)	ϕ
Experiment No. 27								
+ 20 sec.	12.90	1290	1.600	1.445	1.167	2.385	1200	146
+ 30			1.607	1.445	1.170	2.380	1187	146
2 min. 18 sec.			1.605	1.455	1.260	2.320	1300	138
3 min. 48 sec.			1.612	1.454	1.335	2.287	1220	132
5 min. 48 sec.			1.670	1.485	1.467	2.245	1125	127
6 min. 36 sec.		1375	1.740	1.605	1.660	2.090		110
9 min. 42 sec.		1420	1.765	1.640	1.662	2.090		111
10 min. 48 sec.		1415	1.757	1.635	1.650	2.090		111
Experiment No. 28								
+ 1 sec.	11.04	1335	1.285	1.142	0.885	1.960	1105	150
+ 30			1.282	1.175	1.035	1.790	1260	134
1 min.			1.305	1.190	1.147	1.720	1210	125
2 min. 12 sec.			1.327	1.205	1.197	1.695	1212	122
Experiment No. 29								
+ 1 sec.	10.28	1345	1.535	1.320	1.115	2.170	1080	152
+ 48			1.555	1.355	1.300	2.060	1250	133
2 min.			1.550	1.360	1.355	1.985	1310	129
3 min			1.547	1.355	1.345	1.955	1295	129
Experiment No. 35								
+ 20 sec.	15.80	1335	1.589	1.480	1.281	2.320	1220	132
2 min.			1.632	1.500	1.361	2.275	1025	131
3 min. 42 sec.			1.628	1.504	1.360	2.250	1110	130
5 min. 30 sec.			1.622	1.490	1.352	2.260	1010	131
7 min. 30 sec.			1.620	1.498	1.361	2.265	1100	129
14 min. 12 sec.			1.618	1.504	1.357	2.255	1210	130
30 min			1.615	1.498	1.356	2.250	1140	129
Fe-C-Ni (0.85% Ni)								
Experiment No. 45								
+ 21 sec.	12.52	1285	1.586	1.375	1.279	2.165	870	139
+ 42			1.610	1.435	1.381	2.135	1129	128
3 min.			1.656	1.490	1.505	2,000	1321	120
4 min.			1.655	1.485	1.535	2.005	1274	118
6 min.			1.659	1.485	1.542	2.010	1232	117
8 min.			1.662	1.490	1.547	2.005	1258	118
12.2 min.			1.687	1.470	1.565	2.010	942	118
19 min.			1.675	1.480	1.555	1.985	1051	118

continued...

Time After Start of Melting	Mag. of Photo	Temp. °C	x	z	x^1	z^1	γ_{LV} (dynes/cm)	ϕ
			(inches)					
Fe-C-Mn (1.65% Mn)								
Experiment No. 43								
1 min. 24 sec.	12.02	1295	1.810	1.587	1.365	2.515	1302	145
3 min. 30 sec.			1.847	1.595	1.545	2.435	1205	133
6 min.			1.865	1.610	1.585	2.360	1233	133
8 min.		1330	1.870	1.645	1.640	2.345	1452	127
9 min. 30 sec.		1365	1.860	1.605	1.655	2.310	1190	126
11 min.		1385	1.860	1.598	1.655	2.300	1145	126
12.7 min.		1435	1.827	1.585	1.655	2.325	1185	122
14.1 min.		1455	1.831	1.615	1.657	2.310	1380	122
Fe-C-S								
Experiment No. 12 (Data taken from solidified drop)								
+ 11 min.	10.32	1555	0.950	0.800	0.615	1.255	338	165
Experiment No. 36								
1 min. 30 sec.	9.57	1295	1.257	1.035	0.915	1.720	630	156
1 min. 31 sec.			1.257	1.040			638	
32			1.260	1.057			710	
33			1.257	1.051			695	
34			1.257	1.050			690	
35			1.257	1.035			631	
36			1.255	1.035	0.920	1.705	631	155
4 min.		1320	1.250	1.100	0.976		1012	141
4 min.1 sec.			1.247	1.105			1075	
2			1.242	1.095			1019	
3			1.247	1.090			967	
4			1.245	1.090			975	
5			1.242	1.090	0.980		980	141
7 min.		1340	1.265	1.085	1.080		828	132
7 min. 1 sec.			1.255	1.060			738	
2			1.260	1.070			767	
3			1.256	1.055			706	
4			1.255	1.070			782	
5			1.256	1.065			758	
6			1.255	1.075	1.072		807	132
Experiment No. 38								
+ 30 sec.	10.56	1335	1.250	1.125	0.845	1.840	1040	152
1 min. 54 sec.			1.250	1.125	0.843	1.860	1040	153
4 min. 30 sec.			1.255	1.130	0.840	1.870	1059	153
6 min. 30 sec.			1.247	1.135	0.835	1.890	1183	152
8 min. 42 sec.			1.255	1.140	0.837	1.875	1162	153
10 min. 42 sec.			1.250	1.140	0.837	1.880	1205	152

continued....

Time After Start of Melting	Mag. of Photo.	Temp. °C	x	z (inches)	x^1	z^1	γ_{LV} (dynes/cm)	ϕ
Experiment No. 39								
+ 48 sec.	9.55	1295	1.192	1.015	0.912	1.688	704	146
			1.190	1.025	0.887	1.720	780	149
			1.207	1.055	0.920	1.690	930	145
			1.205	1.055		1.710	928	
			1.195	1.065		1.700	1063	
			1.202	1.060		1.725	970	
			1.207	1.050	0.931	1.695	875	143
1 min. 30 sec.			1.205	1.055	0.917	1.680	928	145
			1.205	1.035		1.685	794	
			1.205	1.040		1.700	812	
			1.202	1.030		1.715	758	
			1.205	1.045		1.700	794	
			1.200	1.035		1.768	800	
			1.205	1.040	0.902	1.685	813	146
2 min. 18 sec.		1305	1.205	1.050	0.917	1.700	869	145
4 min.		1285	1.197	1.065	0.905	1.700	1075	143
6 min.			1.200	1.055	0.902	1.700	945	145
8 min.			1.195	1.060	0.895	1.720	1015	145
10 min.			1.195	1.065	0.910	1.705	1082	142
Experiment No. 30		Fe-C-Ce						
5 min. 36 sec.	12.70	1445	1.711	1.455	1.357	2.345	792	141
10 min.		1530	1.735	1.385	1.417	2.185	510	142
12 min.		1620	1.705	1.400	1.405	2.155	590	140
16 min.		1605	1.702	1.380	1.400	2.140	550	141
Experiment No. 31								
3 min.	8.68	1305	1.202	1.045	1.000	1.535	1040	138
6 min. 30 sec.		1375	1.210	1.034	1.012	1.520	907	136
11 min.		1447	1.215	1.005	1.015	1.485	704	138
13 min. 48 sec.		1485	1.205	0.970	1.016	1.470	580	138
19 min. 48 sec.		1615	1.210	0.995	1.055	1.445	650	131
20 min. 54 sec.		1630	1.194	1.030	1.060	1.445	885	127
22 min.		1630	1.192	1.035	1.065	1.437	930	125
Experiment No. 32								
13 min. 48 sec.	8.55	1520	1.010	0.895	0.817	1.420	860	138
16 min. 12 sec.		1635	1.019	0.870	0.825	1.370	615	138
17 min. 18 sec.		1640	1.024	0.900	0.830	1.370	795	138
18 min. 42 sec.		1645	1.010	0.885	0.827	1.380	745	136
Experiment No. 33								
+ 48 sec.	8.45	1315	1.135	0.983	0.919	1.545	940	139
2 min.		1323	1.141	0.980	0.935	1.540	895	139
8 min. 54 sec.		1455	1.190	1.000	0.975	1.565	775	139
14 min. 42 sec.		1535	1.156	0.995	0.945	1.510	880	138
19 min. 36 sec.		1640	1.160	1.000	1.022	1.450	875	128
22 min. 30 sec.		1650	1.127	0.980	1.012	1.380	980	125

continued...

Time After Start of Melting	Mag. of Photo	Temp. °C	x	z	x^1	z^1	γ_{LV}	∅
			(inches)				(dynes/cm)	
Experiment No. 48 (Melting carried out on the nucleating surface)								
1 min. 6 sec.	11.75	1305	1.578	1.360	1.060	2.280	915	160
3 min.		1305	1.567	1.335	1.075	2.260	830	157
4 min. 18 sec.		1405	1.590	1.360	1.110	2.270	855	156
5 min. 30 sec.		1405	1.585	1.370	1.020	2.273	855	157
Experiment No. 50								
10 min.	12.64	1605	1.597	1.325	1.400	1.915	578	130
11 min.			1.595	1.330	1.405	1.910	594	130
12 min.			1.600	1.297	1.402	1.895	500	131
Experiment No. 51								
12 min. 30 sec.	12.35	1600	1.620	1.360	1.300	2.095	660	142
13 min. 30 sec.			1.625	1.370	1.345	2.085	680	136

APPENDIX IV.

Statistical Analysis of Three Fe-C Tests

In each case the drops were taken at 1 second intervals.

Experiment 14

Sequence	γ_{LV}	$(\gamma_{LV} - 1157)$	$(\gamma_{LV} - 1157)^2$
1 - 12	1126	- 31	961
- 24	1134	- 23	529
- 36	1164	+ 7	49
- 48	1438	+281	78961
- 60	1379	+222	49284
- 72	1060	- 97	9490
- 84	1076	- 81	6561
- 96	909	-248	61504
-108	1103	- 54	2916
-120	1034	-123	15129
-132	916	-241	58081
-144	1248	+ 91	8281
-156	1164	+ 7	49
-168	1364	+207	42849
-180	1168	+ 11	121
-192	1295	+138	19044
-204	897	-260	67600
-216	1318	+161	25921
-228	1144	- 13	169
-240	1177	+ 17	289
-252	1242	+ 85	7225
-264	1184	+ 27	729
-276	909	-248	61504
-288	1184	+ 27	729
-300	1006	-151	22801
-312	1199	+ 42	1764
-324	1405	+248	61504
Σ	31,240		603,963

Experiment 19

Sequence	γ_{LV}	$(\gamma_{LV}-1073)$	$(\gamma_{LV}-1073)^2$
1 - 12	979	- 94	8836
- 24	1032	- 41	1681
- 36	970	-103	10609
- 48	1123	+ 50	2500
- 60	989	- 84	7056
- 72	1120	+ 47	2209
- 84	1070	- 3	9
- 96	1370	+297	88209
-108	1370	+297	88209
-120	1031	- 42	1764
-132	1071	- 2	4
-144	979	- 94	8836
-156	1072	- 1	1
-168	994	- 79	6241
-180	1170	+ 97	9409
-192	1122	+ 49	2401
-204	1039	- 34	1156
-216	1006	+ 67	4489
-228	1167	+ 94	8836
-240	1033	- 40	1600
-252	922	-151	22801
-264	979	- 94	8836
-276	1213	+140	19600
-312	941	-132	17424
Σ	25,762		322,716

Experiment 20

Sequence	γ_{LV}	$(\gamma_{LV}-1079)$	$(\gamma_{LV}-1079)^2$
1 -190	1262	+181	32761
-200	964	-115	13225
-210	1231	+152	23104
-220	1282	+203	41209
-230	1052	- 27	729
-240	889	-190	36100
-250	1210	+131	17161
-270	1002	- 77	5929
-280	971	-108	11664
-290	968	-111	12321
-300	1231	+152	23104
-310	993	- 86	7396
-320	1044	+ 35	1225
-330	1212	+133	17689
-340	1140	+ 62	3844
-350	1014	- 65	4225
-360	1031	- 48	2304
-370	1033	- 46	2116
-380	1021	- 58	3364
-390	917	-162	26244
Σ	21,580		285,714

Results of Statistical Treatment

Experiment Number	Mean γ_{LV} (dynes/cm)	Standard Deviation σ (dynes/cm)	$\pm 1\sigma$ Exp. %	Theor. Normal Distn. %	$\pm 2\sigma$ Exp. %	Theor. %
14	1157	150	63	68.2	100	95.46
19	1073	116	79	68.2	92	95.46
20	1079	120	55	68.2	100	95.46

APPENDIX V.

Cooling Rate Considerations

Because the drop samples show a much finer structure in the basal region it is necessary to consider the possible cooling conditions present. One would at first expect a slower cooling rate and hence coarser structure in this region due to the large heat content of the base.

The loss of heat by radiation to the surroundings can be approximated by examining the following model, the dimensions being similar to those used.

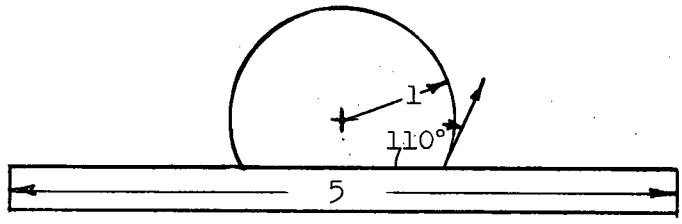

The surroundings are considered to be at a constant low temperature - this is approximately true as the molybdenum susceptor loses its heat extremely rapidly and is black within 2 seconds.

The drop and base plate are considered to be at the same temperature at the instant the power is removed. The drop surface will radiate heat mainly in the 1 direction to the black surroundings.

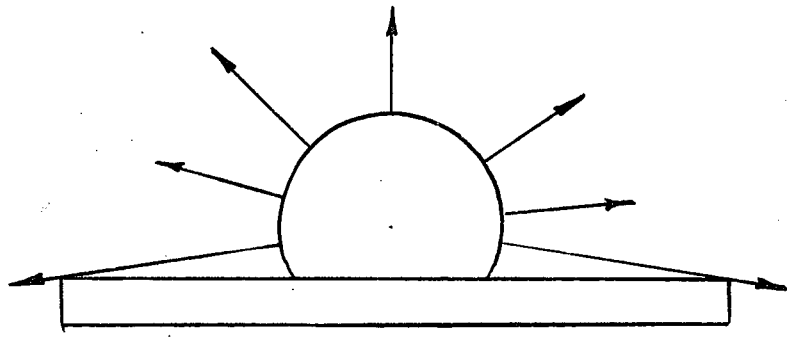

The actual radiating area will be the upper half of the sphere and the small band below the center line.

This angle below the center is:

$$\tan^{-1} \theta = \frac{1 \sin 2\,0^\circ}{2.5} = 0.137\%$$

$$\therefore \quad \theta = 7.83^\circ$$

$$\therefore \quad \text{Area of additional radiating strip} = < 2\pi r \times (1) \left(\frac{7.83 \times 2\pi}{360}\right)$$

$$= < 8.6$$

The surface area involved, considering it as a spheroidal drop, is $< \frac{\pi d^2}{2} + 0.8.6$

(upper half) + (band below the center)

$$= 7.15$$

The plate surface will radiate energy mainly in the direction shown.

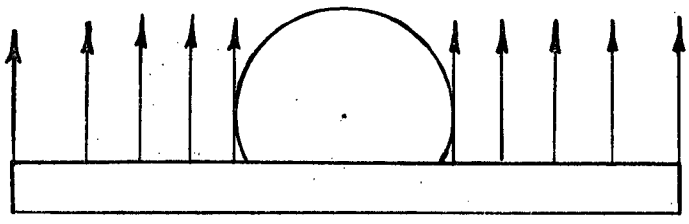

Radiating Area $= 5 \times 5 - \pi(1)^2 = 21.86$

Emissivity of pure iron from 1000°C to 1500°C is approximately 0.36 (Metals Handbook). Emissivity of the graphite plate is $\simeq 0.9$ (Chemistry and Physics Handbook).

The ratio of the heat radiated by the drop surface to that radiated by the graphite base plate is

$$= \frac{\sigma 0.36 \ (T^4 - T_o^4) \ 7.15}{\sigma 0.9 \ (T^4 - T_o^4) \ 21.86} = 0.131$$

where σ is the Stefan's constant
T is the temperature of the radiating body
T_o is the temperature of the surface to which the heat is radiating.

i.e., approximately 1/8 as much heat is radiated by the drop surface. The thermal conductivities of the materials are:

- pure iron at 800°C[37], 0.318 joules/sec/cm^2/°C/cm (This value will decrease with increasing temperature)
- pyrolytic graphite[46] in the basal plane direction, i.e., parallel to the surface, 2 joules/sec/cm^2/°C/cm
- $\perp$ to the surface, 0.02 joules/sec/cm^2/°C/cm

Thus it is quite possible that the direction of maximum heat flow is from the drop and along the graphite surface, being emitted essentially by radiation. This would account for the higher cooling rate in the basal area and the resulting finer structure.

VII. BIBLIOGRAPHY

1. Keverian, J., Taylor, H.F., and Wulff, J., Am. Foundryman 23, 85, (1953).

2. Keverian, J. and Taylor, H.F., Trans. Am. Foundrymen's Soc. 65, 212, (1957).

3. Milman, B.C., Liteinoe Proizv. 6, 11,(1958).

4. White, D.W.G., Canada Department of Mines and Technical Surveys Internal Report No. PM-M-62-4 (May 1, 1962).

5. Uhlig, H.H., in American Society for Metals, "Metal Interfaces". Cleveland, Ohio, The Society (1952), p. 312.

6. Mehl, R.F.,in American Institute of Mining, Metallurgical and Petroleum Engineers, Institute of Metals Div., "The Solidification of Metals and Alloys", N.Y., A.I.M.E. (1951), p. 24.

7. Hollomon, J. H., and Turnbull, D., in American Institute of Mining, Metallurgical and Petroleum Engineers, Institute of Metals Div., "The Solidification of Metals and Alloys", N.Y., A.I.M.E., (1950), p. 1.

8. Turnbull, D.,J. Chem. Phys. 20, 411, (1952).

9. Turnbull, D., and Fisher, J.C., J. Chem. Phys. 17, 71, (1949).

10. Gibbs, J. Willard., "The Collected Works of J. Willard Gibbs", New Haven, Yale Univ. Press (1948).

11. Allen, B.C. and Kingery, W.D., Trans. A.I.M.E. 215, 30,(1959).

12. Kozakevitch, P. and Urbain, G., Rev. Met. 58, 401, 517, and 931,(1961).

13. Dyson, B.F., Trans. A.I.M.E. 227, 1098, (1963).

14. Whalen, T.J., Kaufman, S. M. and Humenik, M., Jr., Trans. Am. Soc. Metals 55, 3,(1962).

15. Koxakevitch, P., Chatel, S., Urbain, G. and Sage, M. Rev. Met. 52, 139,(1955).

16. Kingery, W.D. and Humenick, M., Jr., J. Phys. Chem. 57, 359, (1953).

17. Kaufman, S. M. and Whalen, T.J., Trans. A.I.M.E. 230, 791, (1964).

18. Minkoff, I., Trans. Am. Foundrymen's Soc. 70, 18, (1962).

19. Voronova, N.A., and Mogilevtsev, O.A., Metal. Sci. Heat Treat. Metals (USSR), English Trans. 7, 459, (1963).

20. Boyles, A., "The Structure of Cast Iron", Cleveland, Ohio, American Society for Metals (1947).

21. Morrogh, H. and Williams, W. J., J. Iron Steel Inst. 155, 321 (1947).

22. Loper, C. R., Jr., and Heine, R. W., Trans. Am. Foundrymen's Soc. 69, 583 (1961).

23. Loper, C. R. and Heine, R. W., Trans. Am. Soc. Metals, 56, 135 (1963).

24. Carden, R. L. BCIRA j. 10, 325 (1963).

25. AFS-ASTM Graphite Flake Classification in Grey Cast Iron. ASTM Designation: A 247-47.

26. Garber, S., J. Iron Steel Inst. 181, 291 (1955).

27. Williams, W. J., J. Iron Steel Inst. 164, 407 (1950).

28. Form, G. W. and Wallace, J. F., Trans. Am. Foundrymen's Soc. 70, 1140 (1962).

29. Morrogh, H., Trans. Am. Foundrymen's Soc. 70, 449 (1962).

30. Scheil, E. and Schobel, J.D., Fonderie 192, 73 (1962).

31. Loper, C.R., Jr., Trans. Am. Foundrymen's Soc. 70, 963 (1962).

32. Morrogh, H., BCIRA J. 5, 12, 655 (1955).

33. Strauss, H. E., Von Balchelder, F.W., and Salkovitz, E.I., J. Metals 10, 249 (1951).

34. Bashforth, F. and Adams, J.C., "An Attempt to Test the Theory of Capillary Action", London, Cambridge Univ. Press (1883).

35. Rose, D. J., M.A.Sc. Thesis, University of British Columbia, 1962.

36. Guentert, O.J., J. Phys. Chem. 37, 4, 884 (1962).

37. Smithells, C.J., "Metals Reference Book", 3d ed. London, Butterworths (1962), v. 2, p. 644.

38. Darken, S. L. and Gurry, R.W., "Physical Chemistry of Metals", N.Y., McGraw-Hill (1953).

39. Elliott, J.F., and Gleiser, M., "Thermochemistry for Steelmaking", Reading, Mass. Addison-Wesley Pub. Co. (1960).

40. Elliott, J.F., ed. "The Physical Chemistry of Steelmaking; proceedings", N.Y., Technology Press of M.I.T. and John Wiley (1958).

41. American Institute of Mining and Metallurgical Engineers, Iron and Steel Div. "Basic Open Hearth Steelmaking", 2d ed. N.Y., A.I.M.E. (1951).

42. Bartell, F.E. and Wooley, A.D., J. Am. Chem. Soc. 55, 3518 (1933).

43. Baes, C.F. and Kellogg, H.H., J. Metals 5, 643 (1953).

44. Harvey, J., Clarke, D. and Eastabrook, J.N., Royal Aircraft Establishment Technical Note No. Met. Phys. 361 (1962).

45. Diefendorf, R.J. and Stober, E.R., Metals Progr. 81, 103 (1962).

46. Bradshaw, W. and Armstrong, J.R., "Pyrolytic Graphite, its High Temperature Properties", Lockheed Aircraft Co. Technical Documentary Report No. ASD-TOR-63-195 (1963).

47. Kirkaldy, J.S. and Purdy, G.R., Private Communication (1963).